Cement and Concrete Composites 140 (2023) 105114

Contents lists available at ScienceDirect

Cement and Concrete Composites

journal homepage: www.elsevier.com/locate/cemconcomp

In-situ formation of layered double hydroxides in MgO–$NaAlO_2$-activated GGBS / MSWI BA: Impact of Mg^{2+} on reaction mechanism and leaching behavior

Tao Liu [a,b], Shaohua Li [a], Yuxuan Chen [a], H.J.H. Brouwers [b,c], Qingliang Yu [a,b,*]

[a] School of Civil Engineering, Wuhan University, 430072, Wuhan, PR China
[b] Department of the Built Environment, Eindhoven University of Technology, 5600MB, Eindhoven, the Netherlands
[c] State Key Laboratory of Silicate Materials for Architectures, Wuhan University of Technology, 430070, Wuhan, PR China

ARTICLE INFO

Keywords:
GGBS
MSWI BA
MgO incorporation
$NaAlO_2$ activation
Pore solution
LDHs
Leaching

ABSTRACT

Leaching problems of municipal solid waste incineration bottom-ash (MSWI BA) have been extensively reported in the literature. The outstanding heavy-metal-ion binding capacity of layered double hydroxides (LDHs) can potentially address this problem. This study aimed to investigate the in-situ formation of Mg–Al LDHs in MgO–$NaAlO_2$-activated ground granulated blast-furnace slag (GGBS) and BA blends, and the evolution of pH, ions, reaction products, microstructure, strength, and leaching behavior were characterized. The results indicate that the formation of Mg–Al LDHs is promoted (up to 69.2%) using a higher MgO/$NaAlO_2$ molar ratio, which improves the heavy-metal-ion binding capacity. Simultaneously, the compressive strength increases up to 78.4% with higher MgO/$NaAlO_2$ molar ratios compared to $NaAlO_2$-activated (NA) sample. $Al(OH)_4^-$ reacts with extra Mg^{2+} ions rather than Ca^{2+} ions to preferentially form Mg–Al LDHs over Ca–Al LDHs. Meanwhile, the extra Mg^{2+} ions snatch the $Al(OH)_4^-$ from $Si(OH)_4$, increasing the Mg–Al LDH content and reducing the zeolite content. Moreover, the in-situ-formed LDHs absorbed more SO_4^{2-} than Cl^-.

1. Introduction

Municipal solid waste (MSW) is produced in vast quantities worldwide, and incineration reduces the volume of MSW by up to 90%. However, this process results in a problematic residue, known as municipal solid waste incinerated bottom ash (MSWI BA) [1]. MSWI BA (referred to hereafter as BA for simplicity) is mainly composed of Ca, Si, and Al [2], containing high amount of amorphous silica and alumina, which have pozzolanic properties. Previous studies have demonstrated the potential of BA as a supplementary cementitious material [3]. However, various mobile species may leach out during BA utilization, for example, antimony (Sb), copper (Cu), molybdenum (Mo), thereby contaminating the environment [4]. The crystalline reaction products of alkali-activated materials (AAMs) and calcium silicate hydrate (C–S–H) gels have active sites to absorb heavy-metal ions [5], potentially making them useful for immobilizing heavy-metal ions using BA as a partial precursor. The cations in these gels can chemically exchange with (one to one or one to two in molar ratio) the heavy-metal cations. Simultaneously, the heavy metal-ions can be partially absorbed on the surface of amorphous gels. However, these gels have shown limited capacity to bind heavy metal ions [6].

Layered double hydroxides (LDHs), which are secondary reaction products of alkali-activated ground granulated blast-furnace slag (GGBS) [7], have been demonstrated to possess superior capacity for binding heavy metals [8]. LDHs can be represented as $[M^{2+}_{(1-x)}M^{3+}_x(OH)_2](A^{n-})_{x/n}\cdot zH_2O$, where M represents a metallic skeletal ion (e.g., Mg or Al) and A^{n-} represents an interlamellar anion (e.g., SO_4^{2-} or Cl^-), with various combinations of M^{2+}/M^{3+} possible [9]. However, LDH formation during the alkali activation of GGBS is limited. Enhancing LDH formation in the matrix is a promising method for addressing the leaching of harmful elements from BA in AAMs [10]. The physical surface adsorption of LDHs mainly accounts for its binding capacity [8], with hydroxyl groups on the LDH surface contributing to the coordination of heavy-metal ions [11]. Furthermore, heavy-metal ions such as Cu^{2+} and Cr^{3+} can replace Mg^{2+} and Al^{3+} and intercalate into the framework of LDHs [10]. Xu et al. [12] synthesized and applied Mg–Al–NO3 and Mg–Al–NO2 LDH to AAMs, observing an increase in the

* Corresponding author. School of Civil Engineering, Wuhan University, 430072, Wuhan, PR China.
E-mail address: q.yu@bwk.tue.nl (Q. Yu).

https://doi.org/10.1016/j.cemconcomp.2023.105114
Received 25 September 2022; Received in revised form 20 April 2023; Accepted 30 April 2023
Available online 1 May 2023

chloride binding capacity. However, externally added LDHs absorb significant amounts of water during casting, limiting their dosage in cementitious matrices [13,14]. The promotion of in-situ LDH formation can alleviate this issue. Yang et al. [8] used calcined dolomite in sodium-carbonate-activated GGBS to promote the formation of hydrotalcite-like phases, which exhibited a potentially high ion-binding capacity. Ye [15] investigated the autogenous formation of nitrite- and nitrate-intercalated LDHs. However, the final cementitious matrix contribute little to the chloride binding because of the limited formation of LDHs. Liu et al. [16] observed that sodium aluminate activation can promote the in-situ formation of LDHs, improving the ion-binding capacity of the activated matrix. However, they also observed a relatively slow reaction rate of sodium aluminate activation at an early age, consistent with previous studies [17,18]. The low-pH environment causes a relatively low activating efficiency of $NaAlO_2$, especially at an early age.

The pH of the environment strongly influences the reaction rate, including dissolution of raw materials and the formation of reaction products. It has been reported that the high-pH (>13) environment of AAMs facilitates the leaching of heavy-metal ions. Most metal species in BA (e.g., Cu, Zn, and Pb) follow a cationic leaching pattern, and increasing the pH of the solution leads to a decrease in the concentration of leached elements [19]. However, some heavy-metal ions show an oxyanionic leaching pattern; for example, high concentrations of Mo are reached under highly alkaline conditions [20]. Meanwhile, the leaching of Cl^- and SO_4^{2-} is less pH-dependent, and the released amounts are mainly availability-controlled [21]. It can be hypothesized that the relatively low pH (12–13) of AAMs can alleviate the heavy-metal leaching issue [19]. Therefore, activators with a relatively low pH can promote the formation of Mg–Al LDHs and reduce leaching issues in AAMs. Here, sodium aluminate was introduced as an activator to provide a low-pH environment for the pore solution. The extra available Al–O tetrahedra (denoted as $Al(OH)_4^-$) from sodium aluminate are believed to promote the formation of gels and Mg–Al LDHs [16]. However, Chen et al. [22] reported that although a sodium aluminate activator provided extra $Al(OH)_4^-$ ions, they were coated on the surface of the slag particles. This inhibited the dissolution of the slag particles and negatively influenced the early reaction process, prolonging the setting time. Nonetheless, it promoted the formation of highly crosslinked gels in the late reaction stage, resulting in improved compressive strength. Yliniemi et al. [23] investigated the influence of activator type, including sodium aluminate, on the reaction kinetics, setting time, and compressive strength of alkali-activated mineral wool. Sodium aluminate exhibited lower alkalinity than sodium hydroxide and took several days to initiate the reaction, although it produced a high compressive strength after 28 days of curing. Therefore, mitigation methods are required in terms of slow reaction process at early stage.

To achieve all the aforementioned objectives, that is, (1) the promotion of LDH formation in situ, (2) the need for a low-pH environment, and (3) addressing the slow setting of sodium aluminate activation, the addition of MgO shows potential in alkali activation of GGBS/BA. Mg^{2+} (from MgO) is a divalent cation for Mg–Al LDH formation. MgO can maintain the low-pH environment of the pore solution. Sufficient Mg^{2+} and $Al(OH)_4^-$ (the trivalent cation of Mg–Al LDHs) and their ratios are important for the formation of LDHs [24]. More MgO content can lead to a higher production of hydrotalcite. It can promote the early-stage strength of sodium-aluminate-activated slag/BA (SAASB) as well [25]. However, the presence of extra Mg^{2+} affects the dissolution of the slag particles and results in various reaction products [26]. The variation in dissolved ions from the precursors in the pore solution is important for understanding the reaction mechanism [27–29]. Moreover, the MgO content influences the microstructure of the matrix, purportedly decreasing the formation of calcium aluminosilicate hydrate (C–A–S–H) products with higher Al uptake, high chain length, and a lower degree of crosslinking at a later age. These reactions and microstructural developments rely greatly on the evolution of the pore solution. However, studies on the pore-solution composition in AAMs are scarce, particularly for alkali-activated slag blended with BA [27,29,30]. Studies investigating the effects of Mg^{2+} (from MgO addition) on the reaction and further leaching behavior lack a comprehensive understanding of the MgO–$NaAlO_2$-activated matrix.

This study aims to investigate the impact of Mg^{2+} on the formation LDHs and gel in MgO–$NaAlO_2$-activated GGBS/BA (MSAASB), with special emphasis on the leaching behavior. The pH and alkali-metal ions in the pore solution of the MSAASB were characterized. The reaction products and microstructures were determined, and the leaching of heavy-metal ionss as well as the compressive strengths were tested. Based on the results, the influence of Mg^{2+} on the reaction products and leaching behavior is discussed. These research findings contribute to maximizing Mg–Al LDH formation in situ and its binding to leaching ions.

2. Methods

2.1. Raw materials and sample preparation

GGBS and BA were used in this study. The chemical compositions of GGBS and BA were determined using X-ray fluorescence (XRF) spectroscopy, as shown in Table 1. Magnesia 291 powder (96% purity, Magnesia, Germany) was used in this study. The reactivity of MgO was assessed based on its reaction time with acetic acid [31]. Since the reaction time was 18.95 s, it was classified as medium-active magnesia. The BET specific surface area of MgO was 50.41 m^2/g. The crystalline structures of GGBS, BA, and MgO were determined using X-ray diffraction, as shown in Fig. 1a), b), and c), respectively.

The particle-size distributions (PSD) of the powder feedstocks were determined by laser granulometry using a Master Sizer laser granulometer with an open measuring cell. The powders were prepared by wet dispersion in ethanol. The PSD of GGBS, BA, and MgO are shown in Fig. 1d), with median particle sizes (d_{50}) of 11.839, 11.541, and 9.398 μm, respectively.

GGBS and BA were mixed in a 9:1 (GGBS:BA) mass ratio as the solid precursor, which was activated by sodium hydroxide and sodium aluminate solutions (see the sample IDs in Table 2). The raw starting materials were mixed in the designated proportion in a Hobart mixer following the preparation procedure suggested by EN 196-1 [32]. The pastes were cast in a Ø 45 mm × 55 mm cylindrical plastic mold and then subjected to vibration. All the pastes were sealed and cured at room temperature (20 °C) until the specified curing ages. The mortars were produced by adding a (GGBS + BA)/sand mixture in a ratio of 1:3 by mass. The mortar samples for mechanical testing were cast in a 40 mm

Table 1
Chemical compositions and physical properties of GGBS and BA.

Chemical composition	GGBS (wt. %)	BA (wt. %)	Chemical composition	GGBS (wt. %)	BA (wt. %)
Na_2O	–	5.94	NiO	–	0.02
MgO	8.97	1.92	CuO	–	0.31
Al_2O_3	13.01	8.56	ZnO	–	0.45
SiO_2	31.05	50.05	SeO_2	0.01	–
P_2O_5	–	0.53	SrO	0.06	0.05
SO_3	5.12	0.65	ZrO_2	0.04	0.06
K_2O	0.3	1.06	Ag_2O	0.22	–
CaO	38.82	16.82	Eu_2O_3	–	0.06
TiO_2	1.39	–	PbO	–	0.09
V_2O_5	0.03	0.16	Cl	0.04	0.35
Cr_2O_3	0.02	0.11	LOI[a] (1000 °C)	1.32	5.38
MnO	0.27	0.24	Particle density (g/cm^3)	2.95	2.51
Fe_2O_3	0.67	12.57	–	–	–

[a] LOI = Loss on ignition at 1000 °C.

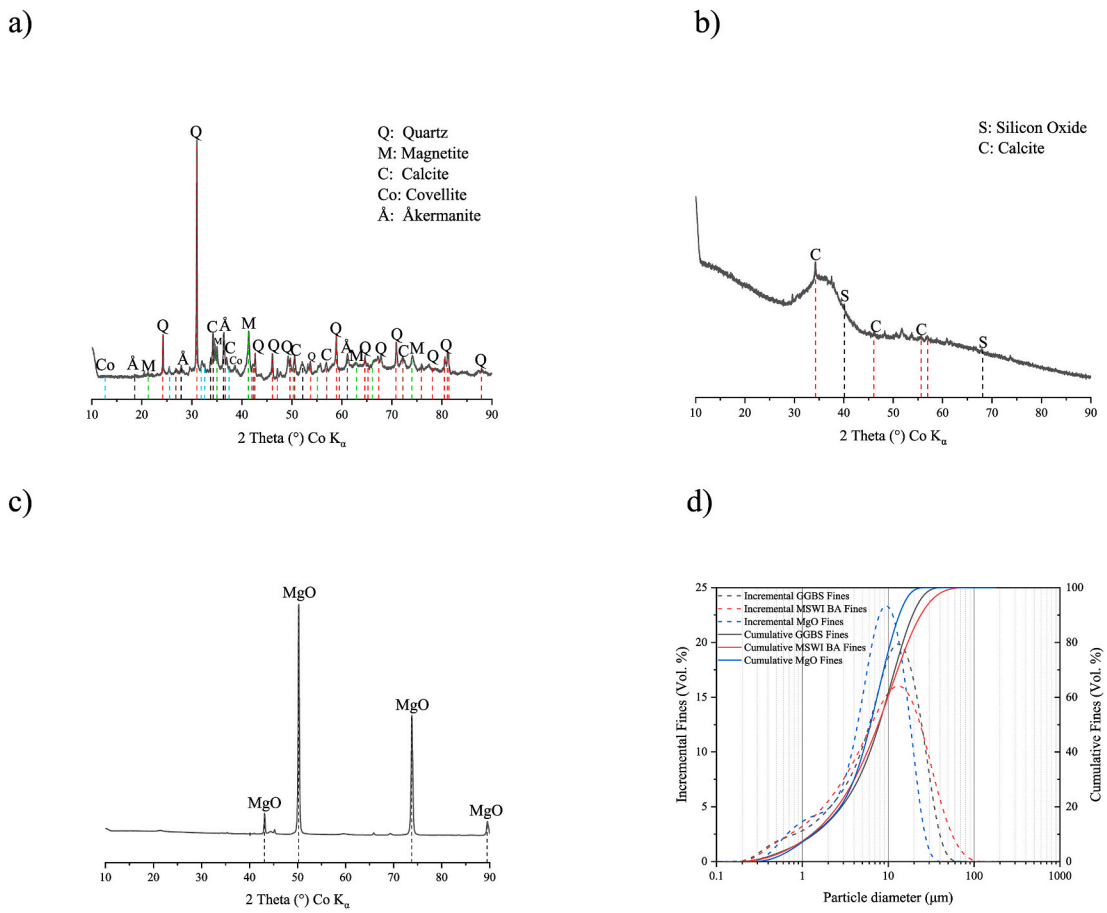

Fig. 1. XRD patterns of a) BA; b) GGBS; and c) MgO; d) Particle size distributions of GGBS, BA, and MgO.

Table 2
Mix design of the pastes (100g binder).

Sample ID	w/b ratio[a]	$NaAlO_2$ (g)	NaOH (g)	MgO (g)	Equivalent Na_2O	GGBS (g)	BA (g)
NH	0.5	–	3.87	–	3	90	10
NA	0.5	7.94	–	–	3	90	10
MA0.5	0.5	7.94	–	1.94	3	90	10
MA1	0.5	7.94	–	3.87	3	90	10
MA2	0.5	7.94	–	7.74	3	90	10
MA4	0.5	7.94	–	15.45	3	90	10

[a] w/b = water-to-binder mass ratio.

× 40 mm × 160 mm prism mold and then subjected to vibration as EN 196-1 [33].

The sodium hydroxide activator was prepared 24 h before preparation for the NaOH-activated (NH) samples. Sodium aluminate activator was prepared 6 h before preparation for the $NaAlO_2$-activated (NA) and MgO–$NaAlO_2$-activated (MA) samples. The additional MgO was calculated based on the aluminate in the activator, where MA0.5, 1, 2, and 4 indicate MgO/$NaAlO_2$ molar ratios of 0.5, 1, 2, and 4, respectively.

2.2. Experimental programs

2.2.1. Cold water extraction

The paste powder was used to measure the cations and pH values of the pore solution by cold water extraction (CWE). The paste powder was sieved by a 200-μm sieve to eliminate the size effect. First, 25 g of powder was mixed with 50 g of deionized water and shaken for 5 min (5 min leaching procedure). The suspension was filtered through a filter syringe. Previous studies have shown no remarkable uptake of ions by filter [34,35]. Finally, the rapid leachate was diluted 10-fold with deionized water. The 25 g diluted solutions were acidified with a few drops of HNO_3 (3 mol/L) to prevent precipitation, and the solutions were analyzed for Na, Ca, Si, Al, and Mg (hereafter denoted as [Na], [Ca], [Si], [Al], and [Mg], respectively) using inductively coupled plasma optical-emission spectrometry (ICP-OES).

Based on the ICP-OES results, the free cation content and pH value of the pore solution were calculated as follows:

$$X = [X]_{CWE} \bullet \frac{m_{105} + m_{add}}{m_{sample}} \quad (1)$$

$$pH = pH_{CWE} + \log\left(\frac{m_{105} + m_{add}}{m_{sample}}\right) \quad (2)$$

where X is the free cation content of the pore solution of the sample (mmol/L); $[X]_{CWE}$ is the concentration of the element in the filtrate obtained after CWE (mmol/L), as determined by ion chromatography (IC) or ICP; m_{105} is the mass of evaporable water at 105 °C in the samples (Table 3); m_{add} is the mass of deionized water added during the 5 min

Table 3
Amount of evaporable water at 105 °C or free water in the paste samples after casting for 28 days.

	Before drying (g)	After drying (g)	m_{105} (g)[a]	$\frac{m_{105}+m_{add}}{m_{sample}}$
NH	25.09	18.63	6.46	2.25
NA	25.04	18.93	6.11	2.24
MA0.5	25.25	19.07	6.18	2.23
MA1	25.00	19.07	5.93	2.24
MA2	25.00	19.38	5.62	2.23
MA4	25.09	20.14	4.95	2.19

[a] The m_{105} value was measured after oven-drying.

rapid-leaching process; m_{sample} is the mass of the sample (g); and pH_{CWE} is the pH of the filtrate obtained after the CWE. Detailed derivations of Eqs. (1) and (2) can be found in Ref. [16].

The CWE technique has a restriction when used to measure pH and ions concentration, however it has been demonstrated that this approach can get a reasonably accurate estimate to anticipate the condition of pore solution. The Na^+, K^+, Ca^{2+}, Mg^{2+}, $Al(OH)_4^-$, and $Si(OH)_4$ had been recommended by using CWE methods in the previous studies [16,34,36].

2.2.2. X-ray diffraction

X-ray diffraction (XRD) was performed using a Bruker D4 Phaser instrument emitting Co-K_α radiation (40 kV, 30 mA). Before the test, the paste samples were ground into powder (<200 μm), immersed in 2-propanol for 24 h to stop the hydration process, and then dried to constant mass at 60 °C for 3 d. The pressed, powdered specimens were measured with a step size of 0.05° and counting time of 1 s/step. The 2θ range was 10–90°. Furthermore, quantification of X-ray diffraction (QXRD) was performed by adding an internal standard (10 wt % Si powder; Siltronix, France) to the paste samples. Then, the mixed paste samples were milled using the XRD mill at level 3 speed for 15 min. For the quantification of mineral phases in the samples, Rietveld analysis was performed using TOPAS software (version 4.2, Bruker) [37]. All TOPAS fitting curves generated in the quantitative XRD analysis are included as supplementary material.

2.2.3. Thermogravimetry

Thermogravimetric (TG) tests were performed on ≈100 mg samples by using an STA 449 F1 instrument at a heating rate of 10 °C/min. The preparation of the powder samples followed the same procedure as XRD analysis. Experiments were carried out from 40 °C to 800 °C, in which N_2 was used as the carrier gas.

2.2.4. Nitrogen physisorption test

Nitrogen physisorption tests were conducted using a TriStar II 3020 (Micromeritics). The pore size distribution was carried out using the Barett, Jonyer, and Halenda (BJH) method [38] from the desorption branch. The preparation of the powder samples was the same with XRD samples.

2.2.5. SEM mapping

The morphologies of the mortar samples at day 28 were analyzed using scanning electron microscopy (SEM). The gold-coated specimens were measured under high vacuum at an accelerating voltage of 15 kV. The SEM instrument was equipped with a secondary electron detector (SED) and energy-dispersive spectrometer (EDS). Then the SEM mapping images were obtained using EDS. The distributions of Si, Al, O, Na, Ca, Mg, and C were determined using EDS mapping.

2.2.6. One-stage batch-leaching test

Batch-leaching tests were performed by subjecting a material with a particle size of <4 mm and L/S ratio of 10 L/kg to demineralized water (EN12457 part 2 [39]). During the one-stage batch-leaching tests, the contact time between the solid material and the leachate was 24 h. After the leaching test, the eluate was filtered through a 0.45 μm filter and further analyzed.

In each test, the material was analyzed for a broad spectrum of parameters using ICP-OES. All eluates were analyzed for Ba, Cr, Cu, Mo, Ni, Se, Sb, V, and Zn. Cl^- and SO_4^{2-} were analyzed using IC.

2.2.7. Mechanical testing

After curing for 28 d, the compressive strength of the mortar samples was determined according to EN 196-1 [32]. The samples were centered on the plates of the machine. Subsequently, the load was increased smoothly at the rate of 2400 N/s over the entire load application until the fracture load.

3. Results

3.1. pH and composition of pore solution

Fig. 2 presents the changes in the pH value and ion concentration with respect to Al, Si, Mg, Na, and Ca in the pore solution of the paste samples at specific curing times of 3, 7, 14, and 28 d. Detailed pore-solution data are listed in the Appendix. The pore solution was dominated by $Al(OH)_4^-$ and Na^+ ions, whereas much lower concentrations of $Si(OH)_4$, Mg^{2+}, and Ca^{2+} were observed. The paragraph with the order of pH, [Al], [Si], [Mg], [Na], and [Ca].

Fig. 2a) illustrates that only the pH of the NH sample exhibits a distinctive decreasing trend with increasing curing age, while the NA and MA samples show stable pH values between 12.80 and 12.95 among the curing ages. The pH decrease in the NH sample was attributed to the consumption of OH^- by the formation of gels and crystalline phases. However, in the NA samples, sodium aluminate shows a pH-buffering effect, and the aluminate continually compensates for OH^- upon the formation of gels and crystalline phases; consequently, the pH remains at ≈12.9. MA1 and MA2 showed a very slight decrease in pH during the first seven days. Subsequently, the continuous hydrolysis of MgO in the pore solution provides Mg^{2+}, promoting the formation of hydrotalcite (Ht). This process was also beneficial for maintaining the pH of the pore solution. Noticeably, with an increase in the $MgO/NaAlO_2$ molar ratio, the rate of decrease in pH before the 7 d mark increased because the extra MgO accelerated geopolymerization and Ht formation [13].

Among the NA and MA samples, a dramatic decrease in [Al] was detected in the pore solution with increasing curing time, whereas the NH sample showed a remarkably low [Al] in the pore solution after three days (Fig. 2b). There is 1935.4 mmol/L [Al] from the initial sodium aluminate activator, while [Al] shows a maximum concentration of around 80 mmol/L in the samples. Because most of Al form gibbsite, a metastable phase, at the early reaction stage, which will be consumed during the curing process. The concentration of $Al(OH)_4^-$ showed an obvious declining trend with increasing $MgO/NaAlO_2$ molar ratio. This can be explained by the fact that extra Mg^{2+} can react with $Al(OH)_4^-$ to form more LDHs. In the NH system, [Al] remains stable at a low value of ≈2.12 mmol/L after 3 d, which is attributed to the intense reaction process within the first 3 d. Low concentrations of available $Al(OH)_4^-$, $Si(OH)_4$, and Na^+ and relatively low-pH environments (compared with the initial pH) indicate a low rate of the reaction process [16]. In the sodium-aluminate-activated system, the NA sample showed the highest [Al] after 3 d. $Al(OH)_4^-$ in the pore solution reacts with $Si(OH)_4$, Mg^{2+}, and Ca^{2+} dissolved from the GGBS. It should be emphasized that the extra $Al(OH)_4^-$ hampers the dissolution of $Si(OH)_4$ from the raw materials [40]. The dissolved $Si(OH)_4$ (from the slag) and extra $Al(OH)_4^-$ ions (from the activator) re-adsorb Ca^{2+} (from the slag) at an early stage, reprecipitating on the surface of the raw materials. The reprecipitated layer was deposited on the grains of the raw materials, delaying further dissolution of the raw materials at an early stage. This resulted in a large amount of $Al(OH)_4^-$ remaining in the pore solution. MA0.5 and MA1

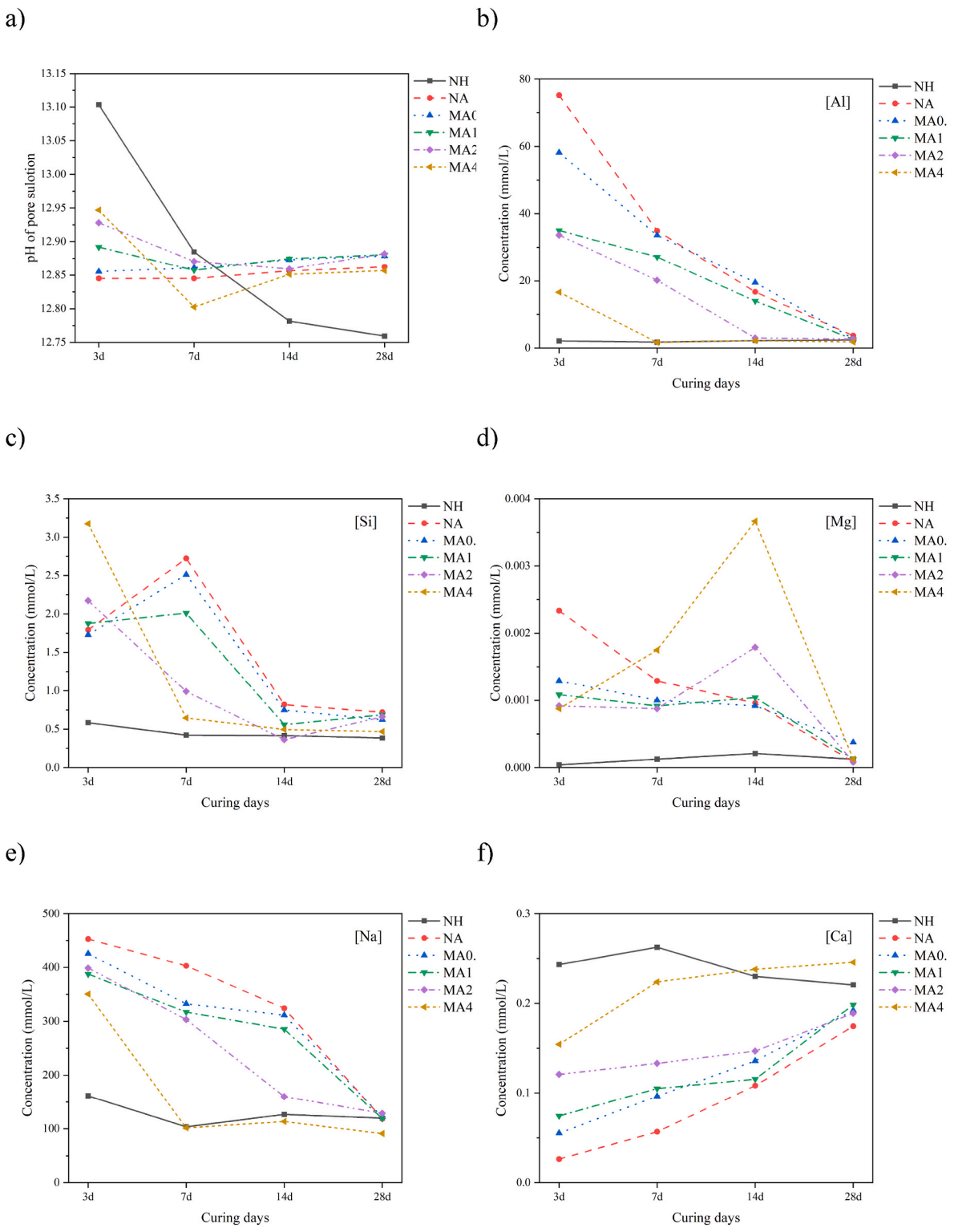

Fig. 2. pH and ion-concentration changes of NH, NA, and MA pore solution at different curing days: a) pH, b) [Al], c) [Si], d) [Mg], e) [Na], and f) [Ca].

exhibited a similar trend to that of NA, where [Al] tended to decrease with increasing MgO content. LDHs were formed in the reactions of Mg^{2+} (produced in the hydrolysis of MgO) with $Al(OH)_4^-$ (provided by the activator). The reaction between Mg^{2+} and $Al(OH)_4^-$ in NA, MA0.5, and MA1 was mainly occurring after 14 d. In addition, the changes of [Al] and [Si] in MA2 indicate that the geopolymerization process is mainly happening between 7 and 14d. The geopolymerization process of MA4 is even faster than that of MA2, as reflected by the complete consumption of [Al] and [Si] within 3–7d. The completion of the MA geopolymerization process can be deduced from the decrease in [Al] to ≈2 mmol/L. Meanwhile, the higher $MgO/NaAlO_2$ molar ratio accelerated the consumption of $Al(OH)_4^-$ in the pore solution to form more gels and LDHs. Besides, the [Al] in MA samples is higher than in NA. Because the MgO maintains the pH of the pore solution at around 12.85–12.9. It is higher than the pH of NA sample at around 12.85. Thus, more Al dissolved from slag, resulting in a higher [Al] in the pore solution than

NA sample.

[Si] varies widely among the NA and MA samples subjected to different curing times (Fig. 2c)). While the [Si] remained low in the NH sample with increasing curing time, which is consistent with the change in [Al]. This confirms the low reaction rate. The [Si] in NA, MA0.5, and MA1 illustrate the hill-like trend with curing time; the [Si] reached a maximum at 7 d and decreased to a low value after 14 d. Large amounts of $Si(OH)_4$ were consumed between 7 and 14 d. This represents a high rate of geopolymerization in $NaAlO_2$-activated materials. For MA2, [Si] decreased dramatically between days 3 and 14. In addition, the [Si] of MA4 decreased as a function of curing time up to 28 d. The decrease in [Si] in MA2 and MA4 occurred earlier than that in the other samples, which is due to the extra MgO in the matrix. As mentioned above, an excessive $Al(OH)_4^-$ content results in a reprecipitated layer. This obstructs the dissolution of $Si(OH)_4$ originating from the GGBS. However, the extra MgO can react with the extra $Al(OH)_4^-$ ions to form hydrotalcite, mitigating the obstruction of $Si(OH)_4$ dissolution. Therefore, the addition of MgO accelerated the geopolymerization process and hydrotalcite formation during the first 7 d. Meanwhile, MA4 exhibits more obvious [Si] changes in the pore solution over days 3–7 than does MA2 during the same timeframe. The noticeably declined pH of MA4 indicates higher reaction rates than those of MA2 during this period. The observable pH shift was a consequence of gelation. During the gelation process, a significant amount of OH^- is consumed, leading to a decrease in pH that slows down the reaction [16].

Fig. 2d) illustrates the changes in [Mg] as a function of the curing age. MA2 and MA4 showed a remarkable increase before 14 d, followed by a dramatic decrease after 14 d. The other samples exhibited a slight decrease with curing time. NH shows stable [Mg] after 3 d, which is in agreement with the changes in [Al] and [Si]. The [Mg] of NA, MA0.5, and MA1 generally decreased with curing time. After the main geopolymerization process, the reaction between $Al(OH)_4^-$ and Mg^{2+} consumes high amount of Mg^{2+} to form hydrotalcite, particularly after 14 d. Meanwhile, MA2 and MA4 showed a high rate of reaction between 7 and 14 d. Large amounts of hydrotalcite were generated in the reaction between $Al(OH)_4^-$ and Mg^{2+} during this period. A higher MgO content accelerated hydrotalcite formation, which is in line with the XRD quantification in Section 3.2.1. The increases in [Mg] in MA2 (after 7 d) and MA4 (after 3 d) were due to the dissolution of MgO. The reaction process consumes large amounts of OH^-, more MgO dissolves in the pore solution to maintain the pH of the environment [41,42].

A significant decrease in [Na] during the curing of the NA and MA samples was observed, while [Na] remained relatively stable in the mixed NH during the curing period (shown in Fig. 2e)). NA, MA0.5, and MA1 showed similar declining trends with increasing curing time. In addition, the higher the $MgO/NaAlO_2$ molar ratio, the lower the [Na]. Moreover, the [Na] in MA2 and MA4 decreased faster than that in NA, MA0.5, and MA1. In addition, the Na^+ in the pore solution of MA showed a variation similar to that of $Al(OH)_4^-$, which indicates that Mg^{2+} accelerated the formation of sodium aluminosilicate hydrate (N–A–S–H) gel to consume excessive Na^+ and $Al(OH)_4^-$, in the pore solution. Mg^{2+} can have a positive contribution on the N–A–S–H formation. It can act as a cross-linker between the silicate and aluminate species, helping to promote the formation of a three-dimensional gel network. This can result in a stronger and more stable gel structure compared to gels formed without Mg^{2+} [43,44]. It is in line with mass loss in terms of gel content presented in Section 3.2.2. It is worth mentioning that the decrease in Na^+ concentration is not associated with zeolite formation, as demonstrated in Section 3.2.1, where it is shown that a higher MgO content in the activation system results in less zeolite formation.

Fig. 2f) shows that during the curing period, the [Ca] of MA continued to increase at a low concentration (below 0.3 mmol/L), while [Ca] in NH remained relatively stable (around 0.25 mmol/L). For the MA pastes, the increase in the $MgO/NaAlO_2$ molar ratio slightly increased [Ca] in the pore solution. MgO addition maintained the pH of the pore solution; consequently, Ca^{2+} from GGBS can be dissolved under a stable pH environment of the pore solution. Therefore, it increased with the curing age.

Overall, [Al] and [Na] in the pore solution show a remarkable decrease with increasing curing age, which is due to the formation of zeolite A and N–A–S–H gels. [Si] decreases with a higher $MgO/NaAlO_2$ molar ratio during curing, reflecting the consumption of $Si(OH)_4$ during the geopolymerization process. Most importantly, the higher MgO content compensates for Mg^{2+} in the pore solution, which accelerates the formation of gels and hydrotalcite. Furthermore, the hydrolysis of the extra MgO maintains the pH environment, which facilitates the dissolution of Ca^{2+} from the GGBS, leading to an increase in [Ca] with curing age.

3.2. Phase evolution of activated pastes

3.2.1. X-ray diffraction

The XRD patterns of the 7- and 28-day NH, NA, and MA paste samples are presented in Fig. 3 a) and b). The content of calcium silicate hydrate (C–S–H, PDF 00-033-0306), calcium aluminum oxide carbonate hydrate (hemi-carbonaluminate, denoted as Hc) ($Ca_4Al_2(OH)_{12}[OH(CO_3)_{0.5}]\bullet 5.5H_2O$, PDF 00-041-0221), and hydrotalcite (denoted as Ht) ($(Mg_6Al_3)CO_3(OH)_{16}\bullet 4H_2O$, PDF 00-014-0191) varied significantly. Quartz (PDF 01-079-1906), akermanite (PDF 01-089-0951), magnetite (PDF 01-089-0951), and calcite (PDF 01-086-2340) from the BA remained relatively unchanged during the curing period.

The reaction products of the paste at 7 d were highly consistent with those of the 28-day pastes. A large amount of Mg–Al LDHs and smaller amounts of Zeolite A (sodium aluminum silicate hydrate; $Na_{96}Al_{96}Si_{96}O_{384}$ $216H_2O$, PDF 00-039-0222), and Hc were the distinct reaction

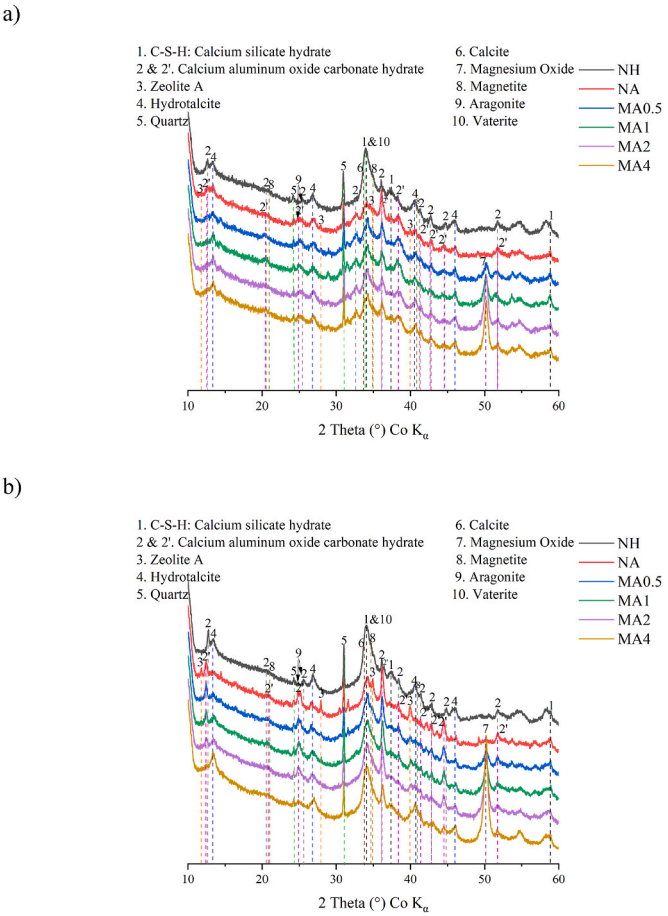

Fig. 3. XRD patterns of NH, NA, and MA pastes at a) 7 d, b) 28 d.

products of NA samples during the initial 7 d. Small amount of zeolite A increased with curing time up to 28 d, while a small amount of C–A–S–H also appeared in the reaction products. This is attributed to the dissolved Ca^{2+} derived from GGBS, which then interacts with $Al(OH)_4^-$ and $Si(OH)_4$ in the pore solution to form C–S–H or C–A–S–H under an alkaline pH environment (higher than 10). In decreasing order, C–S–H, Ht, Hc, and a small amount of zeolite were the primary reaction products of MA samples at 7 and 28 d. The Ht content (Mg–Al LDHs) increased with a higher $MgO/NaAlO_2$ molar ratio. This was associated with the MgO dissolved in the pore solution, and the sufficient Mg^{2+} and extra $Al(OH)_4^-$ (from the activator) accelerated the formation of Mg–Al LDHs. It is worth mentioning that a small amount of Hc (Ca–Al LDHs) was generated after curing for 7 d, while an increasing $MgO/NaAlO_2$ molar ratio hindered the generation of Hc. The solubility of Ht ($K_{SP} = 10^{-66.58}$, 25 °C) is lower than that of Hc ($K_{SP} = 10^{-29.35}$, 25 °C) in an aqueous environment [45,46]. Simultaneously, Mg^{2+} can directly dissolve from the extra MgO, whereas Ca^{2+} originates only from the dissolution of slag particles. Mg^{2+} in the pore solution can reach a higher concentration faster than Ca^{2+}, the precipitation of Ht was easier than that of Hc with higher MgO incorporation. The intensity of the zeolite peak decreases remarkably with an increase in the $MgO/NaAlO_2$ molar ratio in the matrix. The $Al(OH)_4^-$ is prone to react with additional Mg^{2+} instead of Na^+, generating Mg–Al LDHs rather than zeolites. This can also be explained by the fact that low concentrations of [Al] and [Si] are not beneficial to enhancing the crystallinity of sodium aluminosilicate hydrate [47] (here, zeolite A).

Fig. 4 shows the quantification of XRD analysis at 7 and 28 d (details are shown in Table A6 and Table A7). It is noteworthy that the amorphous component is composed of unreacted GGBS, unreacted BA, and C–S–H or calcium(sodium) aluminosilicate hydrate (C(N)–A–S–H) gels [16]. At 7 d, approximately 1.47 wt % Ht was present in the NH paste, while 1.11, 1.13, 1.34, 1.67, and 2.53 wt % Ht existed in the NA, MA0.5, MA1, MA2, and MA4 pastes, respectively. At 28 d, 1.68, 1.61, 1.77, 2.13, 2.33, and 3.04 wt % Ht was detected in the NH, NA, MA0.5, MA1, MA2, and MA4 pastes, respectively. Compared with the Ht content in NH at 28 d, the NA, MA0.5, MA1, MA2, and MA4 pastes showed Ht increases of up to −4.17, 7.84, 26.79, 38.69, and 80.95%, respectively. With curing age, Ht increased only slightly in MA0.5 but remarkably in MA1, MA2, and MA4. The elevated content of MgO significantly promoted Ht formation owing to the extra supply of Mg^{2+}, which is beneficial for reacting with $Al(OH)_4^-$, forming more Ht. This result is in agreement with that of a previous study [48]. Ht in NA is just lower than NH with 4.17%. There will be more Ht generation in NA with further curing ages. At 7 d, 0.32, 0.71, 1.38, and 3.70 wt % of Periclase existed in MA 0.5, MA1, MA2, and MA4, respectively. However, 0.19, 0.44, 1.31, and 2.97 wt % of Periclase were detected in MA 0.5, MA1, MA2, and MA4, respectively. Generally, the content of Periclase decreased with curing ages, which is mainly associated with Ht formation. Most of Ht were formed during 7–28 days as mentioned in Section 3.1.

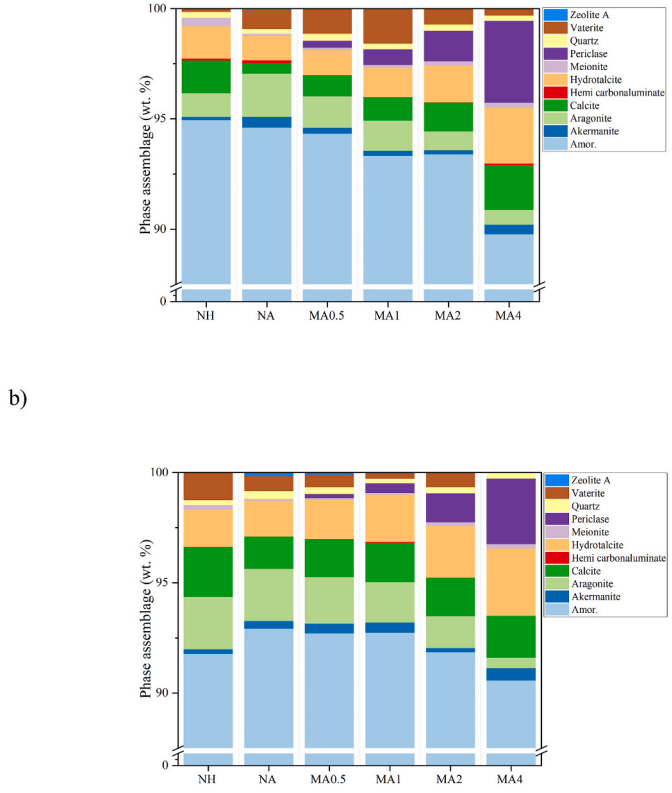

Fig. 4. Quantification of XRD of NH, NA, and MA pastes at a) 7 d and b) 28 d.

Small amounts (0.04 wt %) of zeolite A formed in the NA samples at 7 d and reached 0.16 wt % at 28 d. This increase is ascribed to more $Al(OH)_4^-$ and $Si(OH)_4$ reacting with Na^+ and OH^- ions. At 7 d, MA0.5 and MA1 both contained 0.02 wt % zeolite A, which remained in very low proportions at 28 d. No zeolite A was observed in the NH, MA2, and MA4 pastes at any testing age. It was concluded that MgO in the activating system inhibits the growth of zeolite A.

Calcite, aragonite, and vaterite are three polymorphic forms of calcium carbonate. The calcium-carbonate content of the samples range from 2.69 to 4 wt % at 7 d. The calcium carbonate partly originates from raw BA materials and partly from the carbonation of the samples. At 28 d, the amount of calcium carbonate in the samples is in the range of 3.12–5.88 wt %. The slight increase was caused by carbonation. The increase of calcium carbonate can be observed with a higher content of MgO. Mg^{2+} can stabilize more calcium carbonate (crystalline and amorphous types) [49], which may further influence Ht or Hc formation with its carbonate anions [50]. It is worth to mention that the accuracy of QXRD results may be not sensitive enough to determine the phase assemblages with two decimals. However, those values could be taken as indicator of the trend between different samples.

Considering the capabilities and limitations of QXRD techniques, the phase analysis should be combined with other characterizing approaches. The QXRD using Rietveld refinement are hard to quantify low-content elements [51]. It could be compensated by TG and SEM-EDS. Further discussion about the reaction products will be provided in the following sections.

3.2.2. Thermogravimetric analysis

Fig. 5 illustrates the thermogravimetric (TG) curves and the first derivative of the thermogravimetric curves (DTG) as a function of temperature (40 °C–800 °C) for the different pastes at 7 and 28 d.

For the 7-day pastes, the mass loss and DTG changes of NH and MA4, as presented in Fig. 5a) and b), respectively, are the most obvious among the paste samples. The mass losses of NH and MA4 at 100–300 °C were approximately 5.5 and 7.1 wt %, respectively. This was mainly associated with the dehydration of the C–S–H and C(N)–A–S–H gels [52]. It is notable that the decomposition of Hc [53,54] (at ≈150 °C) and the first-step decomposition of Ht [55] (150–250 °C) occur in the same temperature range of the gels. Also, zeolite A decomposes from 40 °C up to 200 °C [56], which is overlapped by the decomposition of the gels. The NA, MA0.5, MA1, and MA2 samples exhibited mass losses of 5, 5, 5.1, and 5.3 wt % (100–300 °C), respectively. This was mainly associated with the dehydration of the C–S–H and C(N)–A–S–H gels [52]. Simultaneously, small amounts of mass loss result from the decomposition of Hc and zeolite A, along with the first mass loss of Ht, which are also reflected by the XRD patterns and quantification of XRD at 7 d. Notably, the increase in the $MgO/NaAlO_2$ molar ratio contributed to the higher content of gels and Ht (100–300 °C). Most of the mass was lost from gels and Ht because extra Mg^{2+} ions accelerated their formation, which is in agreement with the QXRD results. There is only one distinct peak between 365 and 430 °C, which is assigned to Mg–Al LDHs [57].

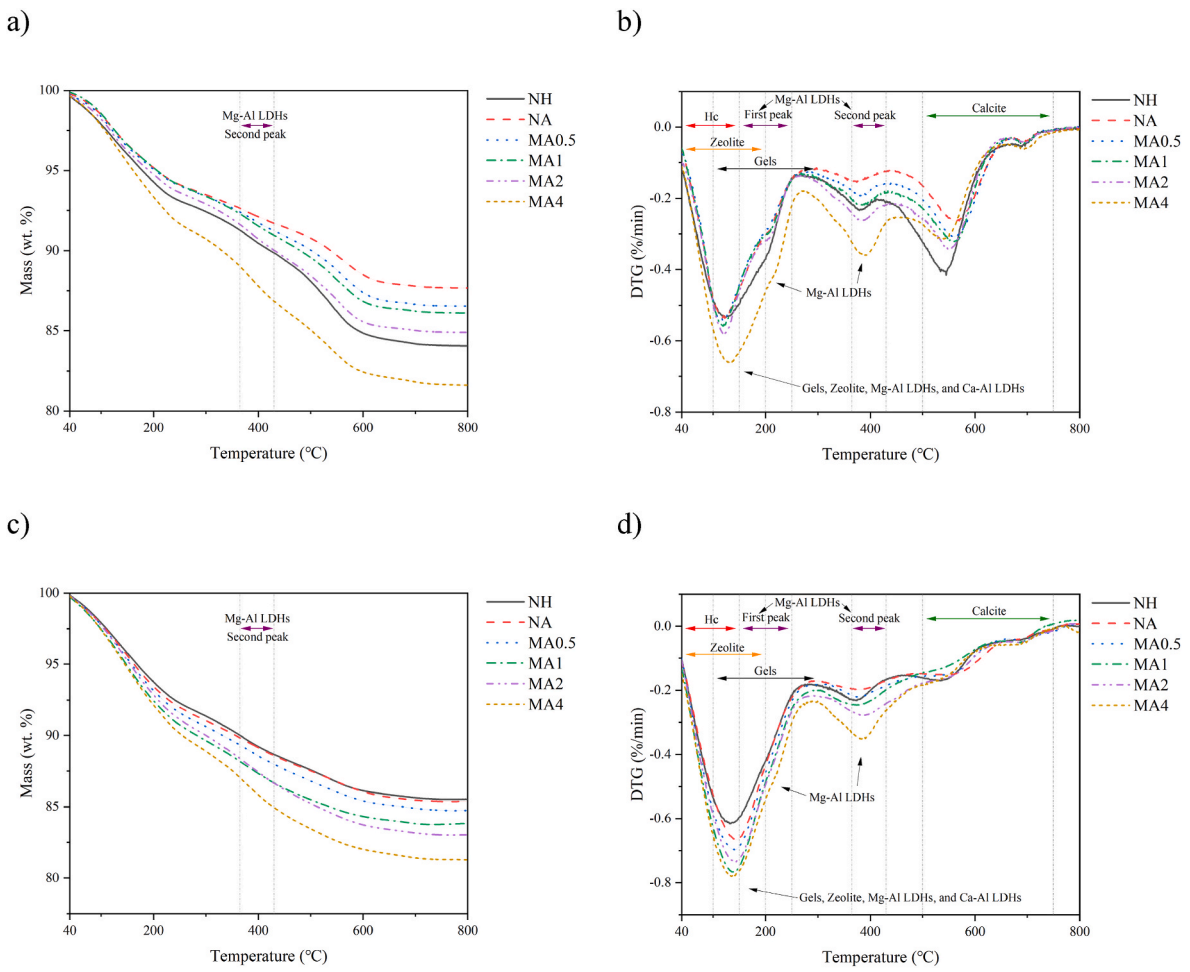

Fig. 5. Mass loss of NH, NA, and MA pastes at a) 7 d and c) 28 d. TGA pattern of NH, NA, and MA at b) 7 d and d) 28 d.

Therefore, this peak was selected to represent the relative contents of Mg–Al LDHs. The weight losses (shown in Table 4) in this temperature range were 1.3, 0.9, 1.2, 1.3, 1.6, and 2.0 wt % for NH, NA, MA0.5, MA1, MA2, and MA4, respectively. The higher mass losses can be attributed to the higher Ht contents. The extra Mg^{2+} (from MgO incorporation) and $Al(OH)_4^-$ (from the activator) are synergistically beneficial for the generation of Ht. Calcium carbonate, which was derived from the raw BA precursors and carbonated pastes in the form of calcite or other polymorphs, decomposes from 500 °C to 750 °C [58,59].

Fig. 5c) and d) illustrate the mass loss and DTG of the 28-day pastes. At temperatures between 100 and 300 °C, the paste samples NH, NA, MA0.5, MA1, MA2, and MA4 underwent mass losses of 6.6, 6.8, 7.2, 7.8, 7.8, and 8.6 wt %, respectively. The Hc and zeolite A contents decrease with a higher $MgO/NaAlO_2$ ratio; the larger mass losses are mainly in the form of bound water in the C–S–H and C(N)–A–S–H gels. Combined with the quantification of the XRD results, the formation of Hc and zeolite A was limited to lower than 0.6 wt % between 7 and 28 d, while the generation of amorphous gels was appreciably promoted. It can be seen that all the NA samples exhibited higher contents of the reaction products at 100–300 °C) than the NH samples. Simultaneously, the amount of Mg–Al LDHs reduced during the second-peak range (shown in Table 4) in the samples were 1.3, 1.3, 1.3, 1.5, 1.8, and 2.2 wt % for NH, NA, MA0.5, MA1, MA2, and MA4, respectively. Compared with the NH reference samples, the changes in the Mg–Al LDH contents were 0, 0, 0, 15.4, 38.5 and 69.2% for NA, MA0.5, MA1, MA2, and MA4, respectively. These results are generally in line with the QXRD results presented in Section 3.2.1. The elevated mass losses are associated with higher Mg^{2+} and $Al(OH)_4^-$ concentrations, which are beneficial for Ht formation. Furthermore, the alkaline environment in the pore solution maintained suitable conditions for the extra Mg^{2+} and $Al(OH)_4^-$ to react with OH^- and CO_3^{2-} to produce more Mg–Al LDHs during curing. For the decomposition of calcium carbonate, two peaks at 550 °C and 700 °C are shown for the 7-day pastes, indicating the coexistence of amorphous and crystalline phases. However, the 550 °C peaks were not observed in the 28-day pastes. The high content of amorphous calcium carbonates in the MA pastes at 7 d is associated with the stabilizing effect of MgO [49]. The less stable form of calcium carbonate tends to transform into a more stable form with increasing curing time [60,61]. This is in line with the QXRD results, where more calcite and aragonite were generated between 7 and 28 d. Correspondingly, less vaterite was observed with increasing curing age.

It is worth mentioning that TGA is a destructive analysis, and the analysis might show certain deviation due to the sample acquisition or volatile components in the sample [62,63]. Therefore, the samples were

Table 4
Relatively average mass losses of LDHs (second peak) during TGA tests.

Sample ID	Mass losses of LDHs (wt. %)			
	7 days	[a]Std	28 days	Std
NH	1.3	0.002	1.3	0.001
NA	0.9	0.021	1.3	0.032
MA0.5	1.2	0.067	1.3	0.087
MA1	1.3	0.076	1.5	0.103
MA2	1.6	0.053	1.8	0.081
MA4	2.0	0.087	2.2	0.015

[a]Std = standard deviation.

tested twice, as shown in the Supplementary part (Fig. SP3 and Fig. SP4). It provides the necessary information to assess the error of the results.

3.3. Microstructural properties

3.3.1. Nitrogen physisorption of activated pastes

The pore size distribution of the pastes at 28 d, as determined by the nitrogen physisorption test, is shown in Fig. 6. Mesopores (2–50 nm) and partial macropores (50–200 nm) were also observed.

Fig. 6a) exhibits the pore size distribution of the paste samples. As can be seen, there is a declining trend with increasing $MgO/NaAlO_2$ molar ratio. The peaks corresponding of the pore size of the NA paste were concentrated at ≈20 nm and ≈40 nm, which were also the largest pore voids among the samples. It is clear that lower pore volumes were associated with higher MgO additions. In particular, the incremental pore volume of MA4 is distinctively lower than that of the NH reference paste. This may be because the high MgO content promotes the formation of gels and Ht-like phases. The increased gel content and Ht-like phases refined the pore structure of the matrices. Furthermore, the microstructure is refined by the evolution of phases during the curing period [64]. Additionally, the microstructural refinement can be attributed to the filler effect of the extra-fine MgO powder. Besides, the large amount of calcium carbonate in NH may refine the pore structure, especially in small size range [65]. Therefore, MA1 and MA2 show coarser pore structure (<100 nm) than NH, which can be related to the reaction products of paste. However, MA1 and MA2 exhibit the denser large size pore structure (>100 nm) than NH. This influences the durability and strength [66]. It is in line with Section 3.5, MA1 and MA2 have a better compressive strength than NH at 28 days.

The cumulative pore volumes of the samples is illustrated in Fig. 6b). With a higher $MgO/NaAlO_2$ molar ratio, a lower cumulative pore volume was obtained. In particular, the cumulative pore volume of sodium-aluminate-activated binders was lower than that of the NH reference pastes after 40 nm. Notably, the cumulative pore volume of MA4 was lower than that of NH for all pore-width ranges. The high bulk MgO content resulted in a significant improvement in the microstructure of the sodium-aluminate-activated binders. Sufficient $Al(OH)_4^-$ and Mg^{2+} ions facilitated the generation of gels and Ht-like phases. Meanwhile, the relatively low-pH environment (≈12.87 according to Section 3.1) is also suitable for the reaction of the amorphous and crystalline phases.

3.3.2. SEM-EDS mapping of activated mortars

The scanning electron microscopy–energy dispersive spectroscopy (SEM-EDS) mappings of the 28-day NH, NA, and MA mortars are presented in Fig. 7. Elemental quantification of Si, Na, O, Al, Ca, Mg, and C is also presented with original SED graphs. The quantitative maps show the differences in the distribution of elements over the SEM mapping graphs. SEM graphs by SED are provided in Fig. SP4.

The most uniform distribution of Na was observed over the particle areas of the samples. Similarly, Si also spreads relatively uniformly over the particle areas, and the sand area is reflected by the high concentrations of Si. For NA, MA0.5, MA1, MA2, and MA4, the distributions of Al and Ca have more overlapping area with an increase in the $MgO/NaAlO_2$ molar ratio. This is attributed to the dissolved Ca^{2+} and $Si(OH)_4$ from GGBS reacting with $Al(OH)_4^-$ (from the activator) to form gels at different curing ages. The geopolymerization process was accelerated by the high concentrations of Mg^{2+} (from additional MgO) in relatively low pH (12–13) activation system [67,68]. In addition, the Mg and Al distributions of MA samples strongly overlap, which is ascribed to the high content of generation of Mg–Al LDHs. This is consistent with the QXRD and TG results. At the same time, a higher Mg/Al ratio indicates a greater possibility of Mg–Al LDH formation. More free Mg^{2+} ions in the matrix promoted the formation of Mg–Al LDHs to fill the pores and cracks, which improved the microstructure of the matrix [69]. This trend is in line with the compressive strength results, as presented in Section 3.5.

3.4. Leaching of heavy-metal ionss

The initial hazard of the powdered raw materials was evaluated using EN 12457–2. Table 5 summarizes the leaching values of raw powdered GGBS and BA, and the limits were established by the Dutch Soil Quality Regulation (SQR) [70] regarding the acceptable emissions for inorganic species. In the raw GGBS particles, all the metal contents were significantly lower than their corresponding legal values, demonstrating that GGBS can be used directly without potential toxicity issues. However, the contents of Cu, Sb, Cl^-, SO_4^{2-} of BA were significantly higher than their legal values.

Table 6 presents the leaching elemental concentration values of the NH, NA, and MA pastes. The alkali-activated GGBS/BA blends considerably decreased the heavy-metal ion leaching concentration as well as the concentrations of chloride and sulfate ions. The contaminants were highly immobilized by these amorphous gels and crystalline LDHs. In the NH samples, all the ions in the leachate were far below their legal limits. However, high concentrations of Se were observed, which were very close to the legal threshold. This is due to the high pH of the pore solution, which results in a high mobility of Se [71]. Once the sodium aluminate activator was applied, the concentration of Se was significantly reduced by up to 56.03% in MA4 compared to NH. This is attributed to the additional formation of Ht in the MA samples, which led to intense Se absorption [72]. The concentration of Ba declined

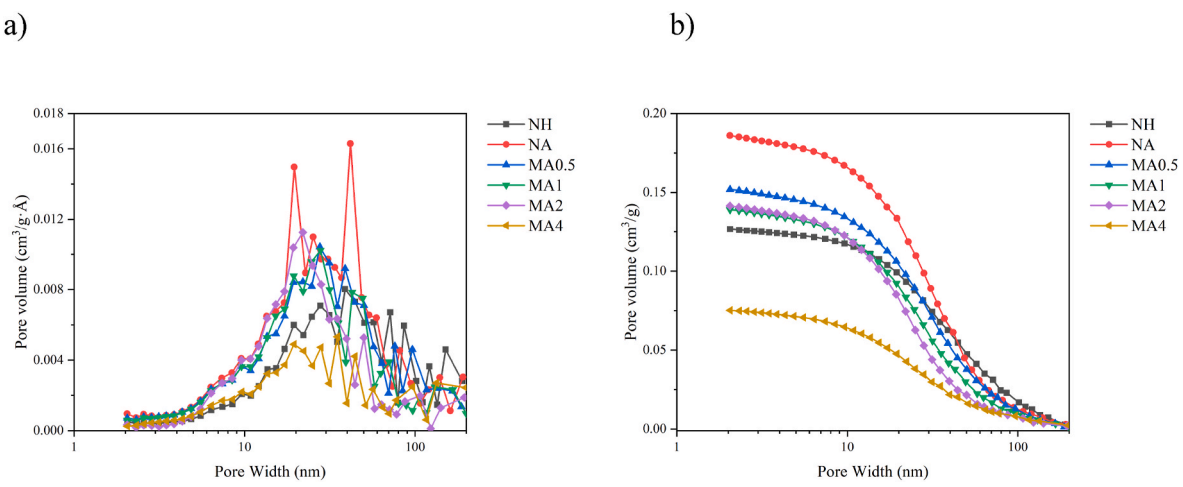

Fig. 6. Pore size distribution at 28 d: a) incremental volume and b) cumulative volume.

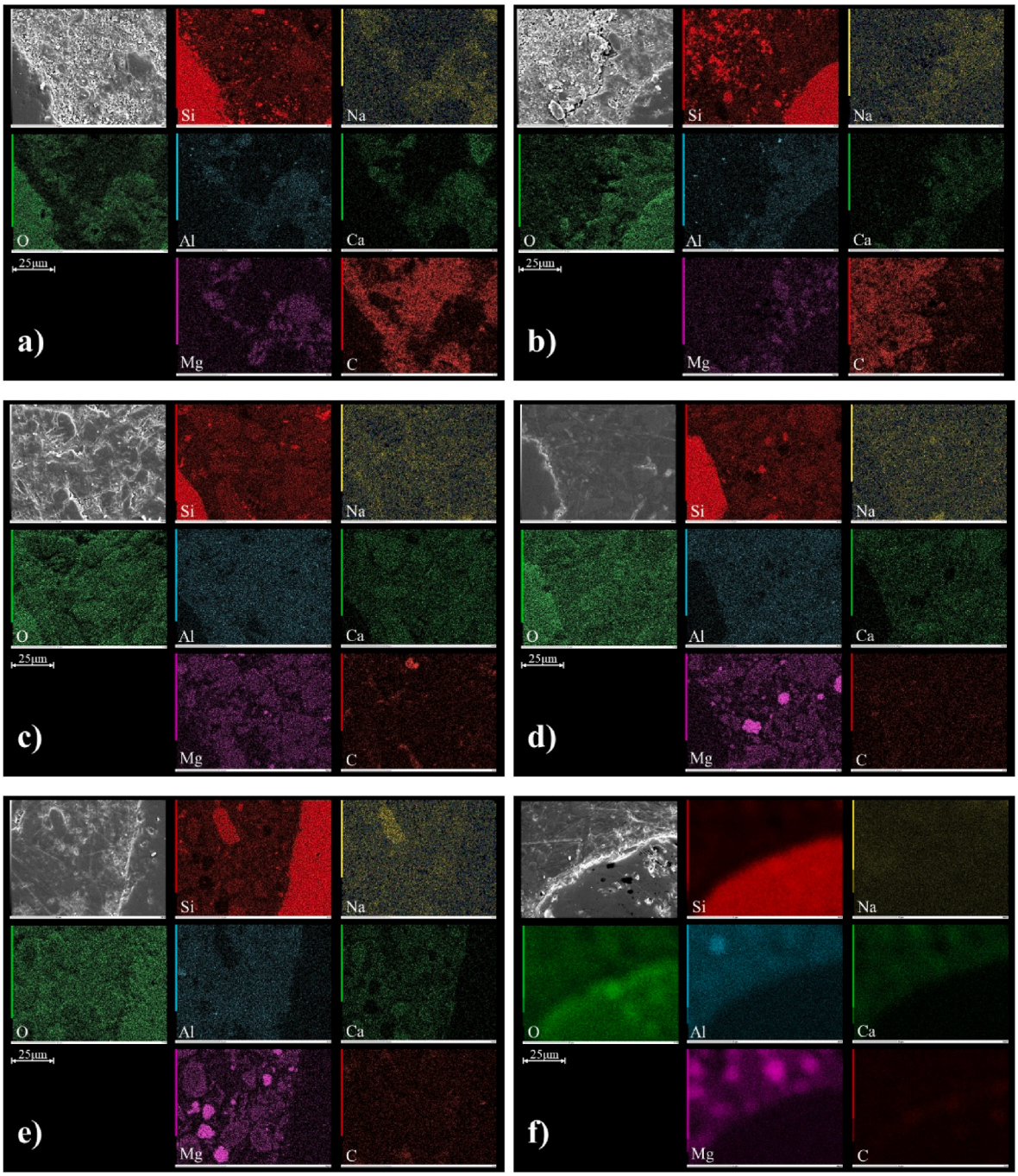

Fig. 7. SEM mapping of NH, NA, and MA mortars at 28 d: a) NH, b) NA, c) MA0.5, d) MA1, e) MA2, and f) MA4.

Table 5
Leaching concentration of raw GGBS and BA (mg/L).

E/I[a]	GGBS	BA	Limit	E/I	GGBS	BA	Limit
Ba	0.075	0.138	22	Sb	0.006	0.401	0.16
Cr	0.030	0.036	0.63	V	0.017	0.003	1.8
Cu	0.002	1.083	0.9	Zn	UDL[b]	UDL	4.5
Mo	0.007	0.732	1	Cl^-	36.2	3354.4	616
Ni	UDL[a]	0.009	0.44	SO_4^{2-}	155	7303.3	1730
Se	0.020	0.013	0.15	pH[c]	11.74	11.40	–

[a] E/I = Elements or ions.
[b] UDL = Under detection limit (<0.001 mg/L).
[c] pH = pH of leachate.

dramatically, that is, by more than 10-fold. The stable pH environment of MA with curing age is beneficial for gel and Ht formation; The elevated gels and Ht formation can effectively immobilize Ba ions, resulting in a lower leaching concentration [73]. In contrast to the leaching ions of raw powdered BA, distinct decreases in Mo, Cl^-, and SO_4^{2-} leaching were observed (Fig. 8). The concentrations of Mo and SO_4^{2-} decreased with increasing $MgO/NaAlO_2$ ratio in the MA samples. On the one hand, the leaching of Mo oxyanions is assumed to be controlled by the dissolution of Ca-containing minerals [74,75], which is related to the solubility of $CaMoO_4$. A lower pH environment of the pore solution is beneficial for controlling the leaching of Mo, as a lower pH results in a higher concentration of Ca^{2+}. Meanwhile, a higher concentration of Ca^{2+} ions existed in the pore solution of the larger MgO matrix, as described in Section 3.1. The high $MgO/NaAlO_2$ ratio favorably

Table 6
28-day leaching concentrations (mg/L) in NH, NA, and MA samples.

E/I[a]	NH	NA	MA0.5	MA1	MA2	MA4	Limit
Ba	0.025	0.002	0.002	0.002	0.004	0.011	22
Cr	UDL[b]	UDL	UDL	UDL	UDL	UDL	0.63
Cu	UDL	UDL	UDL	UDL	UDL	UDL	0.9
Mo	0.077	0.140	0.125	0.109	0.110	0.034	1
Ni	UDL	UDL	UDL	UDL	UDL	UDL	0.44
Se	0.116	0.066	0.054	0.064	0.073	0.051	0.15
Sb	UDL	UDL	UDL	UDL	UDL	UDL	0.16
V	0.089	0.138	0.122	0.107	0.113	0.042	1.8
Zn	UDL	UDL	UDL	UDL	UDL	UDL	4.5
Cl^-	37.802	31.943	33.041	34.275	35.469	44.102	616
SO_4^{2-}	335.589	359.052	274.089	267.540	220.945	166.845	1730
pH[c]	12.27	12.17	12.35	12.35	12.30	12.36	–

[a] E/I = Elements or ions.
[b] UDL = Under detection limit (<0.001 mg/L).
[c] pH = pH of leachate.

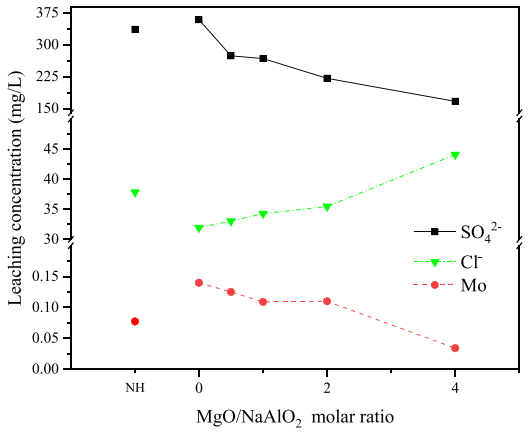

Fig. 8. Effect of $MgO/NaAlO_2$ molar ratio on leaching concentrations of SO_4^{2-}, Cl^-, and Mo.

reduces the leaching of Mo. In addition, SO_4^{2-} leaching is also influenced by Ca^{2+} derived from the precipitation of anhydrite ($CaSO_4$) or gypsum ($CaSO_4 \bullet 2H_2O$) [71].

A small proportion (10 wt %) of effective BA content in the binders resulted in low-level leaching of heavy-metal ions via the dilution effect. Therefore, a correction calculation should be performed to account for the leaching contribution of BA. Thus, the coefficient of the dilution effect was used to calculate the final leaching value contributed by BA, as follows:

$$C_{Dilution} = BA \ / \ (GGBS + BA + MgO + Water + Activator) \quad (3)$$

where $C_{Dilution}$ is the coefficient of the dilution effect, and the unit of all materials is wt. %.

Table 7 lists the leaching elemental concentration values after correcting the dilution effect as well as the $C_{Dilution}$ values. The results were calculated using the following equation:

$$Con_{BA} = \frac{\text{Leaching concentration}}{C_{Dilution}} \quad (4)$$

where Con_{BA} is the leaching value contributed by BA in each paste at 28 d, and the leaching concentration refers to that of the heavy-metal ionss from the paste samples, as listed in Table 6.

As shown in Table 7, the leaching of Mo in the NH sample was similar to that of the raw BA. The hydrated gels can absorb some of the Mo ions; however, the high alkalinity of NH results in high leaching of Mo. However, the leaching of Mo decreases with higher MgO content within the MA samples, which is attributed to the enhanced Ca^{2+} generation. Compared with raw BA, the leaching of Cl^- and SO_4^{2-} significantly declined among the samples, which was associated with the absorption of the gels and LDHs. Compared with the NH samples, a higher MgO addition caused a rise in Cl^- leaching and a reduction in SO_4^{2-} leaching in the MA samples. This was attributed to the higher selectivity of LDHs for SO_4^{2-} ions rather than Cl^- ions in the same pore solution. In addition, Se has a higher leaching potential in MA than in the raw BA. The alkalinity of the activated samples increased Se leaching.

Table 7
28-day leaching concentrations (mg/L) of NH, NA, and MA samples contributed by BA.

E/I[a]	Raw BA leaching	NH	NA	MA0.5	MA1	MA2	MA4
Ba	0.138	0.385	0.032	0.032	0.032	0.067	0.190
Cr	0.036	UDL[b]	UDL	UDL	UDL	UDL	UDL
Cu	1.083	UDL	UDL	UDL	UDL	UDL	UDL
Mo	0.732	1.185	2.222	1.984	1.758	1.833	0.586
Ni	0.009	UDL	UDL	UDL	UDL	UDL	UDL
Se	0.013	1.785	1.048	0.857	1.032	1.217	0.879
Sb	0.401	UDL	UDL	UDL	UDL	UDL	UDL
V	0.003	1.369	2.190	1.937	1.726	1.883	0.724
Zn	UDL	UDL	UDL	UDL	UDL	UDL	UDL
Cl^-	3354.4	581.569	507.032	524.460	552.823	591.150	760.379
SO_4^{2-}	7303.3	5162.908	5699.238	4350.619	4315.161	3682.417	2876.638
$C_{Dilution}$	–	0.065	0.063	0.063	0.062	0.060	0.058

[a] E/I = Elements or ions.
[b] UDL = Under detection limit (<0.001 mg/L).

3.5. Compressive strength

The 3-, 7-, 14-, and 28-day compressive strength of the mortars and the effect of the $MgO/NaAlO_2$ molar ratio on the compressive strength are presented in Fig. 9. The NH samples exhibited a compressive strength of 12.2 ± 0.14 MPa on day 3 and up to 21.2 ± 0.9 MPa at 28 d (as shown in Fig. 9a)). However, the NA samples possessed very low strength (<1.9 ± 0.3 MPa) before 14 d. The low content of the reaction products (especially the amorphous gels, as described in Section 3.2.2) resulted in a less dense matrix. Nevertheless, comparable strengths of up to 20.8 ± 1.3 MPa were observed at 28 d. Large amounts of reaction products were generated in order to develop strength during curing. In addition, the strength increased remarkably between days 14 and 28 in the MA0.5 and MA1 samples. MA0.5 and MA1 show low strengths of ≈2.5 ± 0.1 MPa and ≈6.9 ± 0.3 MPa at day 14, respectively, but high strengths of up to 27.7 ± 1.8 MPa and 29.7 ± 1.8 MPa at 28 d, respectively. Additional MgO has also been reported to promote the strength of the alkali-activated matrix [13,76]. This is attributed to the additional MgO accelerating the formation of Ht and Hc gels. Compared with NA, MA0.5 and MA1 exhibited increases of 33.6% and 42.9%, respectively. In addition, at 28 d, MA2 and MA4 exhibit the highest strengths of 36.9 ± 2.0 MPa and 37.1 ± 1.5 MPa. In contrast with those of NA, growth rates of 77.4% and 78.4% were obtained for MA2 and MA4, respectively. It should be noted that a higher MgO content improves strength development. The strength developments of MA2 and MA4 are in accordance with the generation of the reaction products (Section 3.2). Simultaneously, the strength of the matrices was also in line with the N_2 sorption test (Section 3.3). A higher MgO content leads to a lower porosity, resulting in increased strength.

As can be seen from Fig. 9b), the increase in the $MgO/NaAlO_2$ molar ratio strongly promoted the compressive strength before day 14. The acceleration rate of the $MgO/NaAlO_2$ molar ratio on the strength development exhibited a downward trend after 14 d. It represents that the strength develops intensively around 14 days. It is in agreement with the major geopolymerization process presented in Section 3.1. With the increase in $MgO/NaAlO_2$ molar ratio, the strength increased from 20.7 ± 1.3 MPa to 37.1 ± 1.5 MPa at 28 d in NA matrices.

4. Discussion

4.1. Impact of Mg^{2+} on reaction products

Changes in the ions in the pore solution are critical for understanding the formation mechanism of Mg–Al LDHs. The role of Mg^{2+} in the added MgO was investigated in order to understand the sodium-aluminate activation system. The ion concentration of the pore solutions was used along with XRD, QXRD and TGA to provide an in-depth understanding of the in-situ formation of Mg–Al LDHs. A comprehensive comparison of the concentration changes of Na^+, Ca^{2+}, Mg^{2+}, $Al(OH)_4^-$ from CWE (3, 7, 14, and 28 d) using the Mg–Al LDHs profiles from XRD and QXRD (7 and 28 d) is shown in Fig. 10.

4.1.1. Competition between Mg–Al LDH and Ca–Al LDH formation

The $Mg^{2+}/Al(OH)_4^-$ molar ratio increased, while the $Ca^{2+}/Al(OH)_4^-$ molar ratio decreased with a higher $MgO/NaAlO_2$ molar ratio with increasing curing time in the pore solution of the MA pastes (shown in Fig. 10). Simultaneously, the XRD and QXRD results at 7 and 28 d demonstrated a significant increase in Mg–Al LDH formation (Ht) with a higher $MgO/NaAlO_2$ molar ratio. Meanwhile, reduced formation of Ca–Al LDHs (Hc) was observed with the increase in MgO addition. Fig. 11 shows the dominant mechanism of the extra Mg^{2+} ions on the reaction products of the Mg–Al and Ca–Al LDHs in the sodium-aluminate activation system. The pH environment of the pore solution in the MA samples is stable at ≈12.9 during the curing period. The additional MgO provides sufficient Mg^{2+} in the pore solution; therefore, $Al(OH)_4^-$ favors combination with Mg^{2+} over Ca^{2+} to form Mg–Al LDHs instead of Ca–Al LDHs. Since the solubility product constant of Mg–Al LDHs (K_{SP} = $10^{-66.58}$, 25 °C [45]) is much lower than that of Ca–Al LDHs (K_{SP} = $10^{-29.35}$, 25 °C [46]), the precipitation of Mg–Al LDHs is easier than that of Ca–Al LDHs in the high-Mg/Ca environment in the Al-rich pore solution. Simultaneously, the saturation of Mg–Al LDHs occurs earlier in an aqueous environment with a higher [Mg] in the pore solution, leading to more precipitation of Mg–Al LDHs. In addition, no evidence of M–S–H was detected in the XRD pattern. This is in line with the results of a previous study that demonstrated the absence of Mg-rich silicate gels (e.g. M–S–H) in high-Mg and high-Al systems [77]. Consequently, the increase in Ca^{2+} concentration after 7 days is due to the suitable pH environment in the pore solution dissolving from the slag particles. Mostly, Ca^{2+} participates in the formation of C–S–H and C(N)–A–S–H gels, while Mg^{2+} is barely incorporated into the silicate gels. Therefore, Mg–Al LDHs tend to be the main secondary reaction products instead of Ca–Al LDHs owing to the increased MgO content. Besides, the formation of C–S–H and C(N)–A–S–H gels leads to the reduction of pH in the pore solution after 7 days. This stimulates the dissolution of MgO to provide more Mg^{2+} in the pore solution. Thus, the higher [Mg] can be observed between 7 and 21 days. Simultaneously, more and more Mg^{2+} react with $Al(OH)_4^-$ (from sodium aluminate activator) to form Mg–Al LDHs. It can be observed from QXRD and TG mass losses results at 28 days.

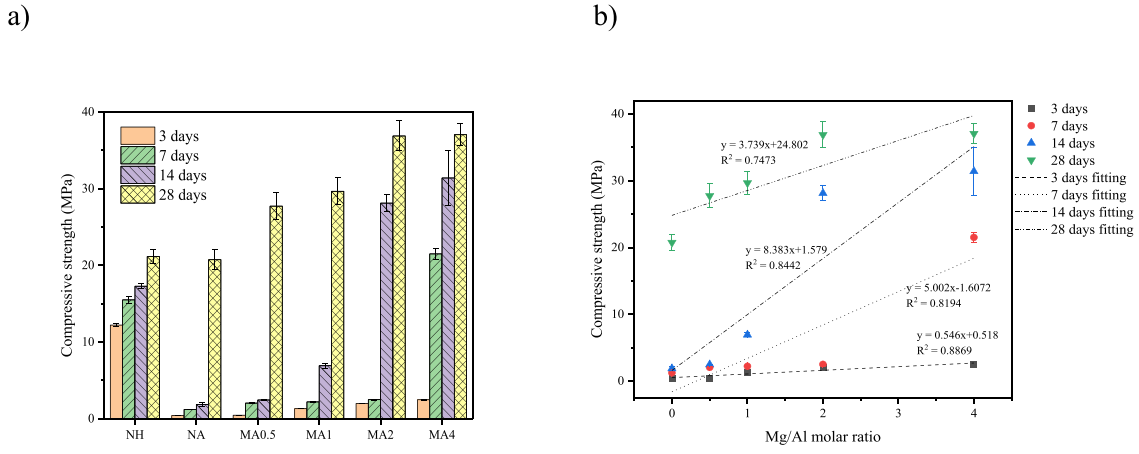

Fig. 9. a) Compressive strength of NH, NA, and MA mortars on specific curing days, and b) the effect of $MgO/NaAlO_2$ molar ratio on compressive strength (excluding the NH sample).

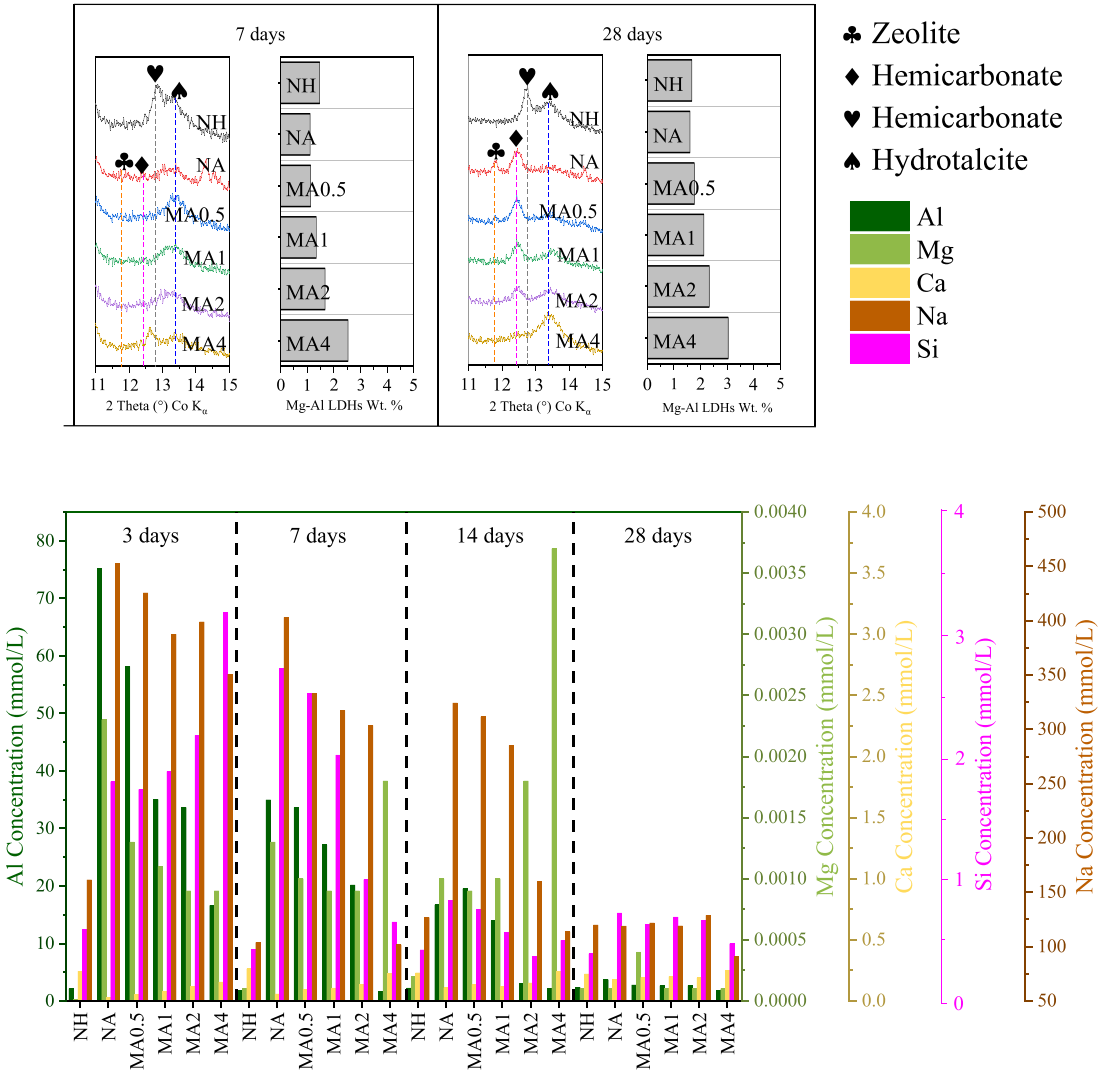

Fig. 10. Mg–Al and Ca–Al LDH formation.

4.1.2. *Competition between Mg–Al LDH and zeolite formation*

Fig. 10 also shows the changes in the Mg^{2+}/$Si(OH)_4$ ratio with different Mg^{2+}/ $Al(OH)_4^-$ molar ratios. The higher the MgO incorporation, the higher the Mg^{2+}/$Si(OH)_4$ ratio in the pore solution before day 14. However, more Mg^{2+} ions were consumed after 14 d. During the period of 14–28 days, the majority of Mg–Al LDHs were generated, as evidenced by TGA patterns showing relatively consistent mass losses (second peak) that align with QXRD results. This further confirms the increase in Mg–Al LDHs during this period. Meanwhile, the presence of zeolite in the XRD patterns increased in the NA samples with curing time. However, the intensity of the zeolite peak decreased with an increase in the MgO/$NaAlO_2$ molar ratio of the raw materials. This is due to the increasing generation of Mg–Al LDHs. In addition, a large amount of Na^+ was consumed to form more N–A–S–H gels after 28 d; therefore, Na^+ decreased with the curing age.

The effect of additional Mg^{2+} on the reaction mechanism for the formation of Mg–Al LDHs and zeolites is presented in Fig. 12. During the curing period, Mg^{2+} maintained a high concentration in the pore solution. The available $Al(OH)_4^-$ bonds with Mg^{2+} to form Mg–Al LDHs in a suitably alkaline environment. Less $Si(OH)_4$ reacts with $Al(OH)_4^-$ and Na^+ to form zeolite owing to more $Si(OH)_4$ forming C(N)–A–S–H gels. Consequently, the extra Mg^{2+} from the added MgO wins the competition against $Si(OH)_4$ in the pore solution. Eventually, the pore solution contains low concentrations of $Al(OH)_4^-$ and $Si(OH)_4$. Meanwhile, the low ion concentrations (i.e., [Al] and [Si]) lead to the low crystallinity of sodium aluminosilicate hydrate [47]. The decrease in zeolite formation can be attributed to the low concentrations of $Al(OH)_4^-$ and $Si(OH)_4$. Therefore, amorphous C(N)–A–S–H gels (low-crystallinity reaction products) can be generated by the extra Na^+ reacting with $Al(OH)_4^-$ and $Si(OH)_4$ at late curing ages. Therefore, C(N)–A–S–H is an alternative reaction product to zeolite in a high-MgO-activated system. Simultaneously, the hump in the XRD pattern (Fig. 10) represents C(N)–A–S–H-type gels rather than zeolite at 28 d.

4.2. *Impact of Mg^{2+} on toxic element binding by in-situ-formed LDHs*

In this study, a one-stage batch leaching test was utilized to investigate the impact of MgO dosage on the leaching behavior of MA pastes. It was found that the leaching concentrations of Mo and SO_4^{2-} were mitigated, whereas those of Cl^- slightly increased with higher MgO

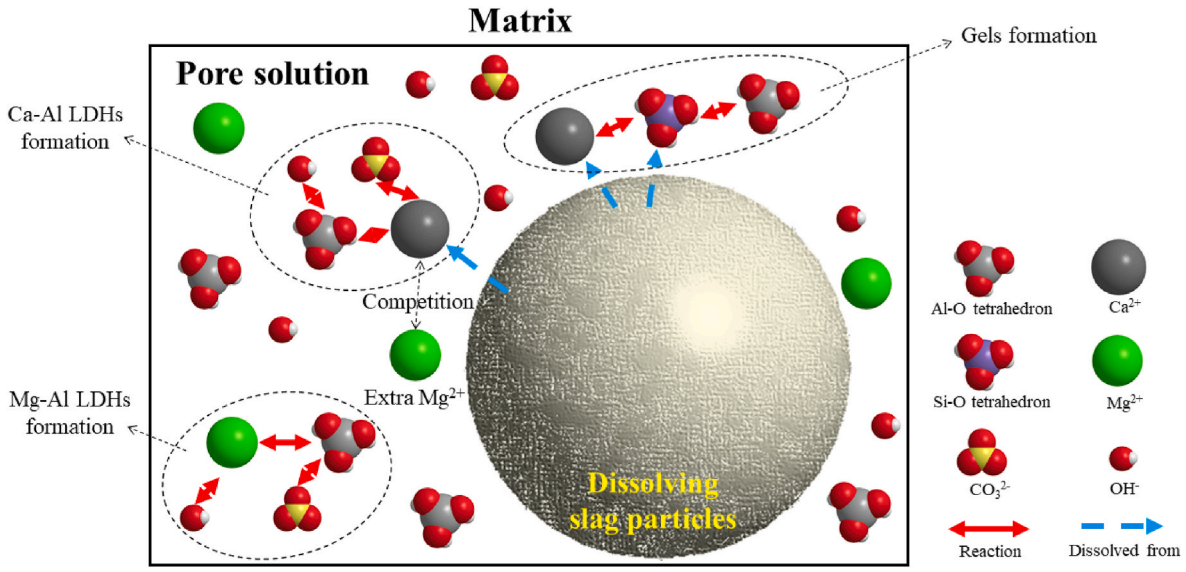

Fig. 11. Competition between Mg–Al and Ca–Al LDH formation in NA and MA sample.

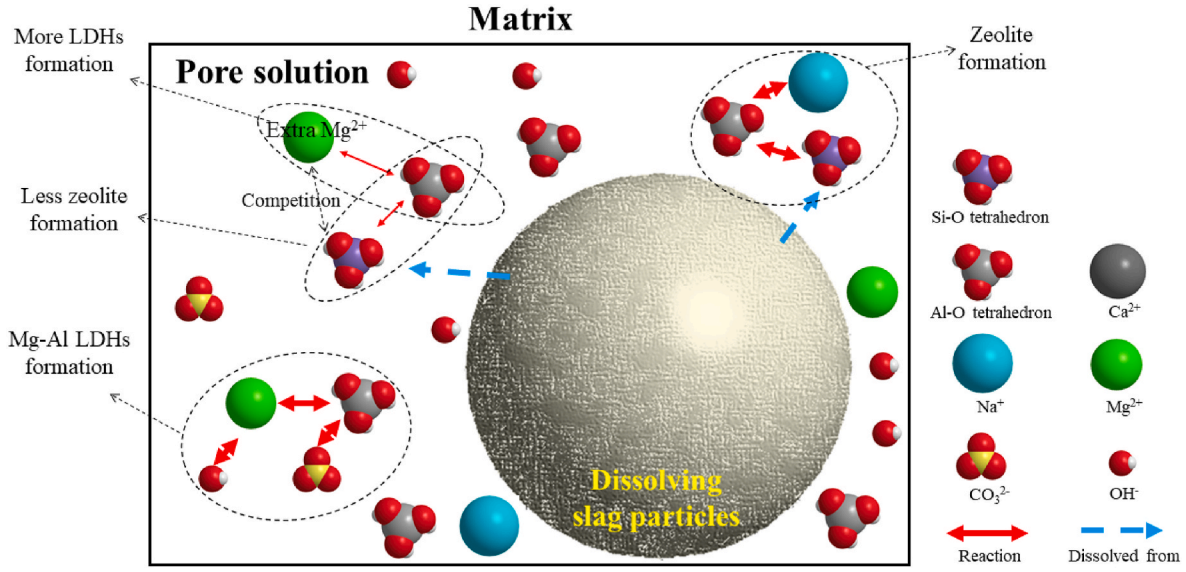

Fig. 12. Competition between Mg–Al LDHs and zeolite formation in NA and MA sample.

content in the sodium-aluminate-activated matrix. The effect of Mg^{2+} on the stabilization of MoO_4^{2-}, Cl^-, and SO_4^{2-} from BA in MA samples is shown in Fig. 13. The higher Mg^{2+} concentration (from extra MgO incorporation) maintained the pH of the pore solution. Therefore, a stable pH environment promoted the dissolution of Ca^{2+} from GGBS during curing (Fig. 10). Simultaneously, the extra Mg^{2+} reacts with $Al(OH)_4^-$ to form Mg–Al LDHs, and less Ca^{2+} reacts with $Al(OH)_4^-$, as discussed above. Therefore, more Ca^{2+} was available in the pore solution. Furthermore, higher [Ca] led to the immobilization of MoO_4^{2-} ions via the formation of $CaMoO_4$. Therefore, it is believed that an increase in Mg^{2+} in the pore solution is beneficial for the immobilization of Mo in Ca-rich precursors.

At the same time, the extra Mg^{2+} creates more in-situ formation of LDHs in the matrix, which affects the leaching behavior of Cl^- and SO_4^{2-}. The affinity of LDHs for SO_4^{2-} is higher than their affinity for Cl^-, so the higher Mg^{2+} concentration results in extra LDH formation; consequently, larger amounts of SO_4^{2-} can be stabilized by the ion exchange of extra in-situ-formed LDHs. However, less Cl^- can be stabilized by the ion exchange of LDHs because more SO_4^{2-} occupies the interlayer sites instead of Cl^-. Although our hypothesis is statistically supported by the promotion of LDHs formed as a result of MgO–$NaAlO_2$ activation, the leaching of Cl^- is higher than that of NH with high MgO incorporation ($MgO/NaAlO_2$ molar ratio >2). It is noteworthy that MA1 exhibits improved leaching of ions, including Cl^- and SO_4^{2-}, and better mechanical properties than NH. Future work should therefore control the $MgO/NaAlO_2$ molar ratio in the sodium-aluminate-activated system to control the in-situ-formed LDHs. Furthermore, this can improve both Cl^- and SO_4^{2-} leaching behaviors. In addition, the incorporation of Mg^{2+} promoted the formation of C(N)–A–S–H in the matrix, which also contributed to the higher surface absorption of toxic elements.

5. Conclusions

This study attempted to understand the effect of the $MgO/NaAlO_2$ molar ratio on MgO–$NaAlO_2$-activated GGBS/BA, with the objective of improving the heavy-metal binding capacity of in-situ-formed LDHs.

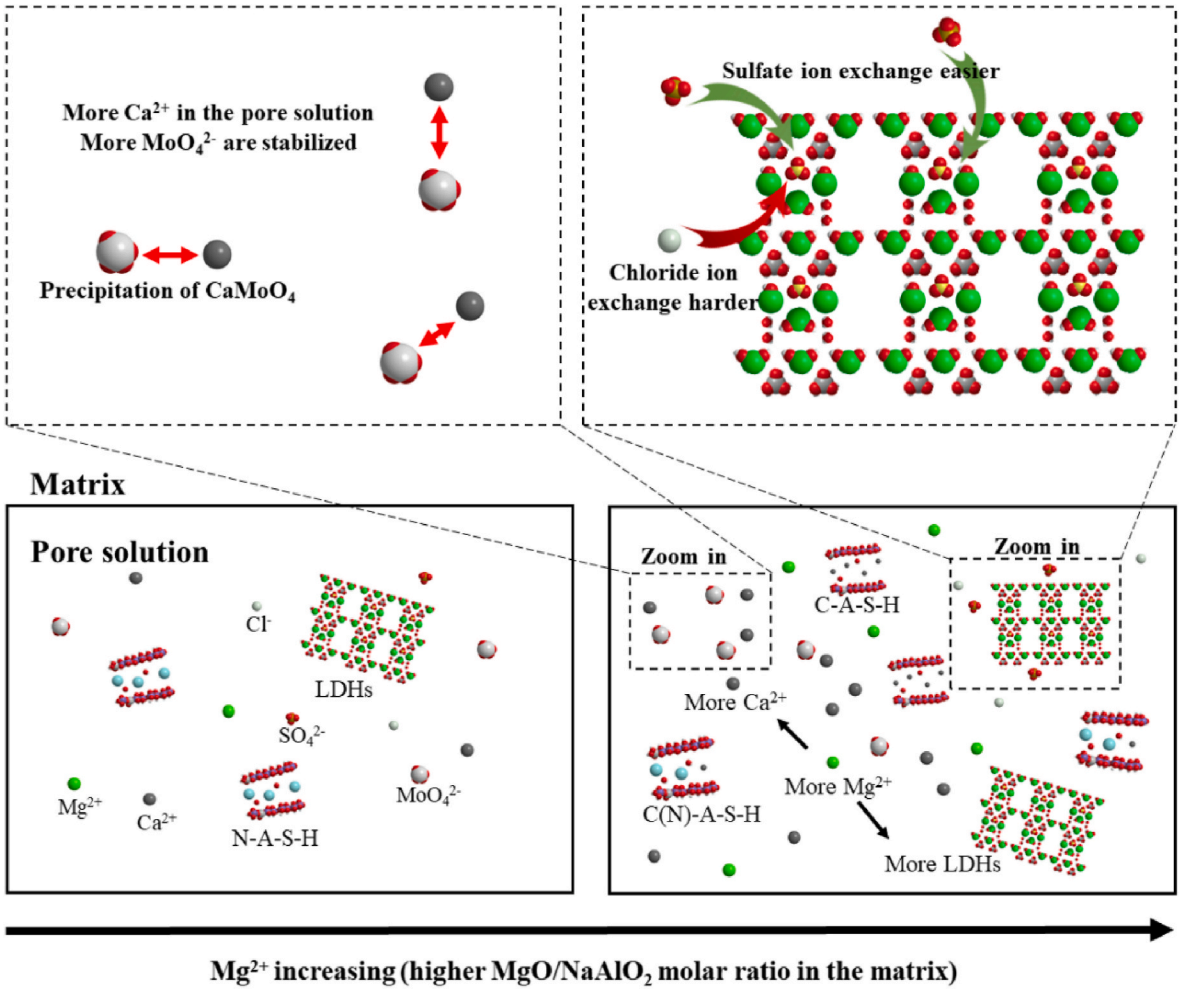

Fig. 13. Impact of Mg^{2+} on leaching of MoO_4^{2-}, Cl^-, and SO_4^{2-} from BA in MgO–$NaAlO_2$-activated slag.

The investigation showed that MgO incorporation maintains the low-pH environment of the pore solution from the early reaction period till 28 days. The additional Mg^{2+} (from MgO powder) and $Al(OH)_4^-$ ions (from the $NaAlO_2$ activator) synergistically promoted the formation of Mg–Al LDHs. From the results and discussion presented above, the following conclusions can be drawn.

- MA showed a significant amount of Mg–Al LDH formation, reaching 3.04 wt % (NH sample is 1.68 wt %) at 28 d. The higher MgO/$NaAlO_2$ molar ratio accelerates the formation of Mg–Al LDHs and gels under relatively low-pH environments (12.80–12.95) during the early reaction period. Furthermore, the higher MgO incorporation transfers the secondary reaction products from Ca–Al LDHs and zeolite to Mg–Al LDHs.
- The microstructure was evidently improved by higher incorporation of MgO. An MgO/$NaAlO_2$ ratio of 4 resulted in the lowest porosity and best mechanical properties. Moreover, the rate of strength growth was accelerated by a higher MgO/$NaAlO_2$ ratio.
- The additional MgO provides extra Mg^{2+}, promoting the reaction between Mg^{2+} and $Al(OH)_4^-$, reducing the reaction between Ca^{2+} and $Al(OH)_4^-$. Meanwhile, less $Al(OH)_4^-$ reacts with Na^+, resulting in less zeolite formation. Mg–Al LDHs tend to be the predominant LDHs (rather than Ca–Al LDHs) in the sodium-aluminate-activated system. Furthermore, zeolite production is impeded by an aqueous environment rich in Mg^{2+}.
- Heavy-metal leaching was significantly decreased by the incorporation of MgO. A lower leachable Mo concentration was obtained owing to the increased formation of $CaMoO_4$. The leaching of SO_4^{2-} decreased dramatically, and the in-situ-formed LDHs absorbed more SO_4^{2-} than Cl^- with elevated MgO addition, owing to the high affinity of LDHs for SO_4^{2-}.

Declaration of competing interest

The authors declare that they have no known competing financial interests or personal relationships that could have appeared to influence the work reported in this paper.

Data availability

Data will be made available on request.

Acknowledgment

This study is supported by the China Scholarship Council (Grant No. 201907720114) and the Eindhoven University of Technology. Special thanks are expressed to A.C.A. Delsing for her help with the ICP analyses. Special thanks are expressed to Mr. Xuan Lin (Building materials group of TU/e) with the TG experiment. Also, special thanks are expressed to Dr. Xinglong Pan and Miss Dongyu Zhang (Stimuli-responsive Functional Materials & Devices group of TU/e), Miss Nadia Boulif (Membrane Materials and Processes group of TU/e) for their help with the SEM mapping.

Appendix A. Supplementary data

Supplementary data to this article can be found online at https://doi.org/10.1016/j.cemconcomp.2023.105114.

Appendix

The pore solution composition data of Al, Si, Mg, Na, and Ca are listed in the following tables, respectively.

Table A1
Concentration of Al (mmol/L)

Sample	Curing days			
	3	7	14	28
NH	2.1234	1.7607	2.2433	2.4057
NA	75.1852	34.9474	16.7144	3.6974
MA0.5	58.1482	33.6204	19.5022	2.7827
MA1	35.0422	27.1274	13.9833	2.6297
MA2	33.6444	20.1656	3.0030	2.6612
MA4	16.6037	1.7040	2.1946	1.8413

Table A2
Concentration of Si (mmol/L)

Sample	Curing days			
	3	7	14	28
NH	0.5837	0.4228	0.4173	0.3853
NA	1.7929	2.7211	0.8193	0.7188
MA0.5	1.7296	2.5118	0.7482	0.6222
MA1	1.8771	2.0111	0.5579	0.6865
MA2	2.1729	0.9918	0.3625	0.6592
MA4	3.1757	0.6452	0.4954	0.4686

Table A3
Concentration of Mg (mmol/L)

Sample	Curing days			
	3	7	14	28
NH	0.0000	0.0001	0.0002	0.0001
NA	0.0023	0.0013	0.0010	0.0001
MA0.5	0.0013	0.0010	0.0009	0.0004
MA1	0.0011	0.0009	0.0010	0.0001
MA2	0.0009	0.0009	0.0018	0.0001
MA4	0.0009	0.0018	0.0037	0.0001

Table A4
Concentration of Na (mmol/L)

Sample	Curing days			
	3	7	14	28
NH	161.4366	103.7492	126.7275	119.8649
NA	452.7518	402.9746	324.2820	118.8610
MA0.5	425.5259	332.6816	311.5509	121.7669
MA1	387.5637	317.4098	285.4848	119.0914
MA2	398.9046	303.4701	160.0295	128.7268
MA4	350.6898	101.6660	113.6112	91.1854

Table A5
Concentration of Ca (mmol/L)

Sample	Curing days			
	3	7	14	28
NH	0.2432	0.2625	0.2299	0.2207
NA	0.0263	0.0567	0.1082	0.1746
MA0.5	0.0551	0.0964	0.1360	0.1921
MA1	0.0743	0.1050	0.1155	0.1985
MA2	0.1209	0.1331	0.1469	0.1889
MA4	0.1544	0.2238	0.2379	0.2458

Table A6
Quantification of XRD results at 7 days (wt. %)

	NH	NA	MA0.5	MA1	MA2	MA4
Akermanitea	0.14	0.49	0.27	0.22	0.19	0.44
Aragonite	1.09	1.96	1.43	1.38	0.84	0.66
Calcite	1.48	0.49	0.97	1.07	1.32	2.03
Hemi carbonaluminate	0.09	0.12	0.00	0.00	0.01	0.07
Hydrotalcite	1.47	1.11	1.13	1.34	1.67	2.53
Meionite	0.38	0.09	0.10	0.11	0.19	0.22
Periclase	0.00	0.00	0.32	0.71	1.38	3.70
Quartz	0.28	0.21	0.31	0.26	0.28	0.24
Vaterite	0.12	0.89	1.12	1.56	0.73	0.33
Zeolite A	0.00	0.04	0.02	0.02	0.00	0.00
Amor.	94.94	94.61	94.33	93.33	93.40	89.79

Table A7
Quantification of XRD results at 28 days (wt. %)

	NH	NA	MA0.5	MA1	MA2	MA4
Akermanite	0.21	0.34	0.44	0.47	0.19	0.57
Aragonite	2.37	2.37	2.11	1.82	1.43	0.48
Calcite	2.28	1.47	1.69	1.79	1.77	1.90
Hemi carbonaluminate	0.00	0.00	0.02	0.04	0.00	0.00
Hydrotalcite	1.68	1.61	1.77	2.13	2.33	3.04
Meionite	0.21	0.09	0.09	0.08	0.17	0.20
Periclase	0.00	0.00	0.19	0.44	1.31	2.97
Quartz	0.22	0.36	0.30	0.20	0.28	0.26
Vaterite	1.23	0.67	0.59	0.26	0.66	0.00
Zeolite A	0.00	0.16	0.08	0.02	0.00	0.00
Amor.	91.79	92.93	92.72	92.74	91.87	90.58

References

[1] P.H. Brunner, H. Rechberger, Waste to energy - key element for sustainable waste management, Waste Manag. 37 (2015) 3–12, https://doi.org/10.1016/j.wasman.2014.02.003.

[2] J.E. Aubert, B. Husson, A. Vaquier, Metallic aluminum in MSWI fly ash: quantification and influence on the properties of cement-based products, Waste Manag. 24 (2004) 589–596, https://doi.org/10.1016/j.wasman.2004.01.005.

[3] X. Gao, B. Yuan, Q.L. Yu, H.J.H. Brouwers, Characterization and application of municipal solid waste incineration (MSWI) bottom ash and waste granite powder in alkali activated slag, J. Clean. Prod. 164 (2017) 410–419, https://doi.org/10.1016/j.jclepro.2017.06.218.

[4] C.H.K. Lam, A.W.M. Ip, J.P. Barford, G. McKay, Use of incineration MSW ash: a review, Sustainability 2 (2010) 1943–1968, https://doi.org/10.3390/su2071943.

[5] Z. Ji, Y. Pei, Bibliographic and visualized analysis of geopolymer research and its application in heavy metal immobilization: a review, J. Environ. Manag. 231 (2019) 256–267, https://doi.org/10.1016/j.jenvman.2018.10.041.

[6] X. Niu, Y. Elakneswaran, C.R. Islam, J.L. Provis, T. Sato, Adsorption behaviour of simulant radionuclide cations and anions in metakaolin-based geopolymer, J. Hazard Mater. 429 (2022), 128373, https://doi.org/10.1016/j.jhazmat.2022.128373.

[7] J.L. Provis, J.S.J. Van Deventer, Geopolymers and other alkali-activated materials, Lea's Chem. Cem. Concr. (2019) 779–805, https://doi.org/10.1016/B978-0-08-100773-0.00016-2.

[8] T. Yang, Z. Zhang, F. Zhang, Y. Gao, Q. Wu, Chloride and heavy metal binding capacities of hydrotalcite-like phases formed in greener one-part sodium carbonate-activated slag cements, in: J. Clean. Prod vol. 253, 2020, https://doi.org/10.1016/j.jclepro.2020.120047.

[9] C. Forano, U. Costantino, V. Prévot, C.T. Gueho, in: Layered Double Hydroxides (LDH), 2013, https://doi.org/10.1016/B978-0-08-098258-8.00025-0.

[10] B. Li, S. Zhang, Q. Li, N. Li, B. Yuan, W. Chen, H.J.H. Brouwers, Q. Yu, Uptake of heavy metal ions in layered double hydroxides and applications in cementitious materials: experimental evidence and first-principle study, Construct. Build. Mater. 222 (2019) 96–107, https://doi.org/10.1016/j.conbuildmat.2019.06.135.

[11] A. Jawad, L. Peng, Z. Liao, Z. Zhou, A. Shahzad, J. Ifthikar, M. Zhao, Z. Chen, Z. Chen, Selective removal of heavy metals by hydrotalcites as adsorbents in diverse wastewater: different intercalated anions with different mechanisms, J. Clean. Prod. 211 (2019) 1112–1126, https://doi.org/10.1016/j.jclepro.2018.11.234.

[12] J. Xu, Y. Song, Y. Zhao, L. Jiang, Y. Mei, P. Chen, Chloride removal and corrosion inhibitions of nitrate, nitrite-intercalated Mg–Al layered double hydroxides on steel in saturated calcium hydroxide solution, Appl. Clay Sci. 163 (2018) 129–136, https://doi.org/10.1016/j.clay.2018.07.023.

[13] T. Liu, Y. Chen, Q. Yu, J. Fan, H.J.H. Brouwers, Effect of MgO, Mg-Al-NO3 LDH and Calcined LDH-CO3 on chloride resistance of alkali activated fly ash and slag blends, Construct. Build. Mater. 250 (2020), 118865, https://doi.org/10.1016/j.conbuildmat.2020.118865.

[14] Z.Y. Qu, Q.L. Yu, H.J.H. Brouwers, Relationship between the particle size and dosage of LDHs and concrete resistance against chloride ingress, Cement Concr. Res. 105 (2018) 81–90, https://doi.org/10.1016/j.cemconres.2018.01.005.

[15] H. Ye, Autogenous formation and smart behaviors of nitrite- and nitrate-intercalated layered double hydroxides (LDHs) in Portland cement-metakaolin-

dolomite blends, Cement Concr. Res. 139 (2021), https://doi.org/10.1016/j.cemconres.2020.106267.
[16] T. Liu, Q. Yu, H.J.H. Brouwers, In-situ formation of layered double hydroxides (LDHs) in sodium aluminate activated slag: the role of Al-O tetrahedra, Cem, Concr. Res. 153 (2022), https://doi.org/10.1016/j.cemconres.2021.106697.
[17] H. zhe Jiao, S. fei Wang, A. xiang Wu, H. ming Shen, J. dong Wang, Cementitious property of NaAlO2-activated Ge slag as cement supplement, Int. J. Miner. Metall. Mater. 26 (2019) 1594–1603, https://doi.org/10.1007/s12613-019-1901-y.
[18] B. Chen, J. Wang, J. Zhao, Mitigating the drying shrinkage and autogenous shrinkage of alkali-activated slag by NaAlO2, Materials 13 (2020), https://doi.org/10.3390/MA13163499.
[19] H. Luo, Y. Cheng, D. He, E.H. Yang, Review of leaching behavior of municipal solid waste incineration (MSWI) ash, Sci. Total Environ. 668 (2019) 90–103, https://doi.org/10.1016/j.scitotenv.2019.03.004.
[20] D. Nordmark, A. Lagerkvist, Controlling the mobility of chromium and molybdenum in MSWI fly ash in a washing process, Waste Manag. 76 (2018) 727–733, https://doi.org/10.1016/j.wasman.2018.03.016.
[21] M.J. Quina, J.C.M. Bordado, R.M. Quinta-Ferreira, The influence of pH on the leaching behaviour of inorganic components from municipal solid waste APC residues, Waste Manag. 29 (2009) 2483–2493, https://doi.org/10.1016/j.wasman.2009.05.012.
[22] B. Chen, J. Wang, J. Zhao, Effect of sodium aluminate dosage as a solid alkaline activator on the properties of alkali-activated slag paste, Adv. Mater. Sci. Eng. 2021 (2021), https://doi.org/10.1155/2021/6658588.
[23] J. Yliniemi, B. Walkley, J.L. Provis, P. Kinnunen, M. Illikainen, Influence of activator type on reaction kinetics, setting time, and compressive strength of alkali-activated mineral wools, J. Therm. Anal. Calorim. 144 (2021) 1129–1138, https://doi.org/10.1007/s10973-020-09651-6.
[24] H.N. Yoon, S.M. Park, H.K. Lee, Effect of MgO on chloride penetration resistance of alkali-activated binder, Construct. Build. Mater. 178 (2018) 584–592, https://doi.org/10.1016/j.conbuildmat.2018.05.156.
[25] Z. Wang, S. Park, H.R. Khalid, H.K. Lee, Hydration properties of alkali-activated fly ash/slag binders modified by MgO with different reactivity, J. Build. Eng. 44 (2021), 103252, https://doi.org/10.1016/j.jobe.2021.103252.
[26] S.A. Bernal, R. San Nicolas, R.J. Myers, R. Mejía De Gutiérrez, F. Puertas, J.S.J. Van Deventer, J.L. Provis, MgO content of slag controls phase evolution and structural changes induced by accelerated carbonation in alkali-activated binders, Cem, Concr. Res. 57 (2014) 33–43, https://doi.org/10.1016/j.cemconres.2013.12.003.
[27] Y. Zuo, M. Nedeljković, G. Ye, Pore solution composition of alkali-activated slag/fly ash pastes, Cement Concr. Res. 115 (2019) 230–250, https://doi.org/10.1016/j.cemconres.2018.10.010.
[28] X. Ke, S.A. Bernal, J.L. Provis, Uptake of chloride and carbonate by Mg-Al and Ca-Al layered double hydroxides in simulated pore solutions of alkali-activated slag cement, Cement Concr. Res. 100 (2017) 1–13, https://doi.org/10.1016/j.cemconres.2017.05.015.
[29] M. Nedeljković, B. Ghiassi, S. van der Laan, Z. Li, G. Ye, Effect of curing conditions on the pore solution and carbonation resistance of alkali-activated fly ash and slag pastes, Cement Concr. Res. 116 (2019) 146–158, https://doi.org/10.1016/j.cemconres.2018.11.011.
[30] S. Song, H.M. Jennings, Pore solution chemistry of alkali-activated ground granulated blast-furnace slag, Cement Concr. Res. 29 (1999) 159–170, https://doi.org/10.1016/S0008-8846(98)00212-9.
[31] M.A. Shand, The chemistry and technology of Magnesia, Chem. Technol. Magnesia (2006) 1–266, https://doi.org/10.1002/0471980579.
[32] EN196-1, Methods of testing cement - Part 1: determination of strength, Eur. Stand. (2005) 1–33.
[33] EN 196-1, en 196-1, EN 196-1 ed. 2015-08-01 methods test. Cem. Part 1 determ, Strength 1 (2011) 46.
[34] G. Plusquellec, M.R. Geiker, J. Lindgård, J. Duchesne, B. Fournier, K. De Weerdt, Determination of the pH and the free alkali metal content in the pore solution of concrete: review and experimental comparison, Cement Concr. Res. 96 (2017) 13–26, https://doi.org/10.1016/j.cemconres.2017.03.002.
[35] K. De Weerdt, G. Plusquellec, A. Belda Revert, M.R. Geiker, B. Lothenbach, Effect of carbonation on the pore solution of mortar, Cement Concr. Res. 118 (2019) 38–56, https://doi.org/10.1016/j.cemconres.2019.02.004.
[36] T. Liu, In-situ Formation of Layered Double Hydroxides (LDHs) in Alkali Activated Materials (AAMs), Thesis, Eindhoven University of Technology, 2023.
[37] A.A. Coelho, TOPAS and TOPAS-Academic: an optimization program integrating computer algebra and crystallographic objects written in C++: an, J. Appl. Crystallogr. 51 (2018) 210–218, https://doi.org/10.1107/S1600576718000183.
[38] Influence of pozzolans and slag on the microstructure of partially carbonated cement paste by means of water vapour and nitrogen sorption experiments and BET calculations, Cement Concr. Res. 40 (2010) 1723–1733, https://doi.org/10.1016/j.cemconres.2010.08.014.
[39] BS EN 12457-2, Characterisation of Waste - leaching - Compliance Test for Leaching of Granular Waste Materials and Sludges - Part 2: one stage batch test at a liquid to solid ratio of 10 l/kg for materials with particle size below 4 mm (without or with size reduction), BSI Stand. Publ. 3 (2014) 30.
[40] K.C. Newlands, M. Foss, T. Matschei, J. Skibsted, D.E. Macphee, Early stage dissolution characteristics of aluminosilicate glasses with blast furnace slag- and fly-ash-like compositions, J. Am. Ceram. Soc. 100 (2017) 1941–1955, https://doi.org/10.1111/jace.14716.
[41] D.A. Vermilyea, The dissolution of MgO and Mg(OH)[sub 2] in aqueous solutions, J. Electrochem. Soc. 116 (1969) 1179, https://doi.org/10.1149/1.2412273.
[42] W. C.L, J.S.J. de, S. C.A, N. N.-Y.T, M. O, L. H, Dissociation of magnesium oxide and magnesium hydroxide nanoparticles in physiologically relevant fluids, J. Nanoparticle Res. 20 (2018), https://doi.org/10.1007/s11051-018-4314-3.
[43] X. Ke, V.A. Baki, A.I. Large, G. Held, B. Walkley, J. Li, Atomic-scale characterisation of sodium aluminosilicate hydrates (N-A-S-H) and Mg-substituted N(-M)-A-S-H using XANES, Appl. Geochem. 147 (2022), https://doi.org/10.1016/j.apgeochem.2022.105515.
[44] M. Bedeaux, J.P. Gevaudan, B. Lama, W.V. Srubar, Atomic structure and phase assemblages in novel M-(N)-A-S-H materials, Cement Concr. Res. 142 (2021), https://doi.org/10.1016/j.cemconres.2020.106336.
[45] E. Bernard, W.J. Zucha, B. Lothenbach, U. Mäder, Stability of hydrotalcite (Mg-Al layered double hydroxide) in presence of different anions, Cement Concr. Res. 152 (2022), https://doi.org/10.1016/j.cemconres.2021.106674.
[46] T. Matschei, B. Lothenbach, F.P. Glasser, Thermodynamic properties of portland cement hydrates in the system CaO–Al2O3–SiO2–CaSO4–CaCO3–H2O, Cement Concr. Res. 37 (10) (2007) 1379–1410, https://doi.org/10.1016/j.cemconres.2007.06.002.
[47] Q. Li, Y. Zhang, Z. Cao, W. Gao, L. Cui, Influence of synthesis parameters on the crystallinity and Si/Al ratio of NaY zeolite synthesized from kaolin, Petrol. Sci. 7 (2010) 403–409, https://doi.org/10.1007/s12182-010-0085-x.
[48] M. Ben Haha, B. Lothenbach, G. Le Saout, F. Winnefeld, Influence of slag chemistry on the hydration of alkali-activated blast-furnace slag - Part I: effect of MgO, Cement Concr. Res. 41 (2011) 955–963, https://doi.org/10.1016/j.cemconres.2011.05.002.
[49] A.E. Morandeau, C.E. White, Role of magnesium-stabilized amorphous calcium carbonate in mitigating the extent of carbonation in alkali-activated slag, Chem. Mater. 27 (2015) 6625–6634, https://doi.org/10.1021/acs.chemmater.5b02382.
[50] Z. Chen, H. Ye, The role of CaO and MgO incorporation in chloride resistance of sodium carbonate-activated slag, Cem. Concr. Compos. 132 (2022), https://doi.org/10.1016/j.cemconcomp.2022.104625.
[51] M. Mohebbi, F. Rajabipour, E. Madadian, A framework for identifying the host phases in Coal-derived fly ash, Fuel 314 (2022), https://doi.org/10.1016/j.fuel.2021.122806.
[52] T. Liu, Q. Yu, H.J.H. Brouwers, X. Fan, Utilization of waste glass in alkali activated slag/fly ash blends: reaction process, microstructure, and chloride diffusion behavior, J. Sustain. Cem. Mater. 12 (2023) 516–526, https://doi.org/10.1080/21650373.2022.2082577.
[53] S. Berger, C.C.D. Coumes, P. Le Bescop, D. Damidot, Influence of a thermal cycle at early age on the hydration of calcium sulphoaluminate cements with variable gypsum contents, Cement Concr. Res. 41 (2011) 149–160, https://doi.org/10.1016/j.cemconres.2010.10.001.
[54] F. Song, Z. Yu, F. Yang, Y. Liu, Y. Lu, Strätlingite and calcium hemicarboaluminate hydrate in belite-calcium sulphoaluminate cement, Ceram. - Silikaty. 58 (2014) 269–274.
[55] C. Forano, U. Costantino, V. Prévot, C.T. Gueho, Layered Double Hydroxides (LDH) Chapter 14.1, 2013.
[56] N.M. Musyoka, L.F. Petrik, E. Hums, A. Kuhnt, W. Schwieger, Thermal stability studies of zeolites A and X synthesized from South African coal fly ash, Res. Chem. Intermed. 41 (2015) 575–582, https://doi.org/10.1007/s11164-013-1211-3.
[57] E.S. Zhitova, S.V. Krivovichev, I. Pekov, H.C. Greenwell, Crystal chemistry of natural layered double hydroxides. 5. Single-crystal structure refinement of hydrotalcite, [Mg6Al2(OH)16](CO3)(H2O)4, Mineral. Mag. 83 (2019) 269–280, https://doi.org/10.1180/mgm.2018.145.
[58] E.R. McCaslin, C.E. White, A parametric study of accelerated carbonation in alkali-activated slag, Cem, Concr. Res. 145 (2021), https://doi.org/10.1016/j.cemconres.2021.106454.
[59] T. Liu, J. Fan, Z. Peng, Mechanical properties, dry shrinkage, and water penetration of reusing fine and ultrafine recycled concrete aggregate, Materials 15 (2022), https://doi.org/10.3390/ma15248947.
[60] B. Jones, Review of aragonite and calcite crystal morphogenesis in thermal spring systems, Sediment. Geol. 354 (2017) 9–23, https://doi.org/10.1016/j.sedgeo.2017.03.012.
[61] L.E. Wasylenki, P.M. Dove, J.J. De Yoreo, Effects of temperature and transport conditions on calcite growth in the presence of Mg2+: implications for paleothermometry, Geochem. Cosmochim. Acta 69 (2005) 4227–4236, https://doi.org/10.1016/j.gca.2005.04.006.
[62] D. Dollimore, Thermal analysis, Anal. Chem. 66 (1994) 17–25, https://doi.org/10.1021/ac00084a002.
[63] P.J. Haines, Principles of thermal analysis and calorimetry, Igarss 2014 (2014) 1–5.
[64] O. Burciaga-Díaz, I. Betancourt-Castillo, Characterization of novel blast-furnace slag cement pastes and mortars activated with a reactive mixture of MgO-NaOH, Cement Concr. Res. 105 (2018) 54–63, https://doi.org/10.1016/j.cemconres.2018.01.002.
[65] L. Cheng, Y. Chen, B. Yuan, Q. Yu, The underlying role of sodium tripolyphosphate on the cementitious mechanism of calcium carbonate binder, Compos. B Eng. 247 (2022), https://doi.org/10.1016/j.compositesb.2022.110362.
[66] M.R. Ahmad, L.P. Qian, Y. Fang, A. Wang, J.G. Dai, A multiscale study on gel composition of hybrid alkali-activated materials partially utilizing air pollution control residue as an activator, Cem. Concr. Compos. 136 (2023), https://doi.org/10.1016/j.cemconcomp.2022.104856.
[67] H. Sreenivasan, E. Adesanya, H. Niu, P. Perumal, A.M. Kantola, V.V. Telkki, M. Huttula, W. Cao, J.L. Provis, M. Illikainen, P. Kinnunen, Evidence of formation of an amorphous magnesium silicate (AMS) phase during alkali activation of (Na-Mg) aluminosilicate glasses, Cement Concr. Res. 145 (2021), https://doi.org/10.1016/j.cemconres.2021.106464.

[68] B. Akturk, M. Abolfathi, S. Ulukaya, A.B. Kizilkanat, T.J.N. Hooper, L. Gu, E. H. Yang, C. Unluer, Hydration kinetics and performance of sodium carbonate-activated slag-based systems containing reactive MgO and metakaolin under carbonation, Cem. Concr. Compos. 132 (2022), https://doi.org/10.1016/j.cemconcomp.2022.104617.

[69] B. Li, Q. Li, W. Chen, Spatial zonation of a hydrotalcite-like phase in the inner product of slag: new insights into the hydration mechanism, Cement Concr. Res. 145 (2021), https://doi.org/10.1016/j.cemconres.2021.106460.

[70] Dutch Soil quality regulation. https://rwsenvironment.eu/subjects/soil/legislation-and/soil-quality-decree/, 2006.

[71] Y. Zhang, B. Cetin, W.J. Likos, T.B. Edil, Impacts of pH on leaching potential of elements from MSW incineration fly ash, Fuel 184 (2016) 815–825, https://doi.org/10.1016/j.fuel.2016.07.089.

[72] Q. Tian, B. Guo, K. Sasaki, Immobilization mechanism of Se oxyanions in geopolymer: effects of alkaline activators and calcined hydrotalcite additive, J. Hazard Mater. 387 (2020), https://doi.org/10.1016/j.jhazmat.2019.121994.

[73] X. Huang, C. Xin, J. shan Li, P. Wang, S. Liao, C.S. Poon, Q. Xue, Using hazardous barium slag as a novel admixture for alkali activated slag cement, Cem. Concr. Compos. 125 (2022), https://doi.org/10.1016/j.cemconcomp.2021.104332.

[74] G. Cornelis, C.A. Johnson, T. Van Gerven, C. Vandecasteele, Leaching mechanisms of oxyanionic metalloid and metal species in alkaline solid wastes: a review, Appl. Geochem. 23 (2008) 955–976, https://doi.org/10.1016/j.apgeochem.2008.02.001.

[75] Q. Alam, M.V.A. Florea, K. Schollbach, H.J.H. Brouwers, A two-stage treatment for Municipal Solid Waste Incineration (MSWI) bottom ash to remove agglomerated fine particles and leachable contaminants, Waste Manag. 67 (2017) 181–192, https://doi.org/10.1016/j.wasman.2017.05.029.

[76] F. Jin, K. Gu, A. Al-Tabbaa, Strength and hydration properties of reactive MgO-activated ground granulated blastfurnace slag paste, Cem. Concr. Compos. 57 (2015) 8–16, https://doi.org/10.1016/j.cemconcomp.2014.10.007.

[77] S.A. Walling, S.A. Bernal, L.J. Gardner, H. Kinoshita, J.L. Provis, Phase Formation and evolution in Mg(OH)2-Zeolite cements, Ind. Eng. Chem. Res. 57 (2018) 2105–2113, https://doi.org/10.1021/acs.iecr.7b04201.